Magnetic properties of epitaxial ferrite thin films grown on a substrate with trigonal symmetry

Ritesh Patel

May 2018

Magnetic properties of epitaxial ferrite thin films grown on a substrate with trigonal symmetry

Ritesh Patel

Doctoral Program in Applied Physics

Submitted to the Graduate School of
Pure and Applied Sciences
in Partial Fulfillment of the Requirements
for the Degree of Doctor of Philosophy in
Engineering
at the
University of Tsukuba

Table of Contents

Abstract

Ferrimagnetism is seen in some ferromagnetic oxides with complex structures. Ferrimagnetic materials have shown the potential for a wide range of applications because of their good insulating properties, high magnetic anisotropy, moderate saturation magnetization, high Curie temperature and low microwave losses. In this study, we report on the growth and magnetic properties of cobalt ferrite (111) and barium hexaferrite (0001) epitaxial thin films, deposited on α-Al_2O_3(0001) substrates by radio frequency magnetron sputtering. The characteristic features of cobalt ferrite and barium hexaferrite are high magnetocrystalline anisotropy, moderate saturation magnetization, moderate coercivity and high ferromagnetic resonance frequency. Previous reports suggest obtaining perpendicular magnetic anisotropy in cobalt ferrite and barium hexaferrite thin films is a tough task. In order to grow those ferrite thin films with the better quality, we used the reactive RF magnetron sputtering technique which is capable of producing films of nanometer thickness, high purity, and smoother surface. Thus it overcomes the limitations in growing good quality thin films of other deposition techniques, such as molecular beam epitaxy, chemical vapor deposition, liquid phase epitaxy, and pulsed laser deposition technique.

The $Co_xFe_{3-x}O_4$ (CFO) (111) epitaxial thin films are deposited by optimizing parameters such as different growth temperature, oxygen flow rate, and thickness. The obtained thin films show perpendicular magnetic anisotropy at higher oxygen flow rate (9 sccm) and temperature (600 ℃). The perpendicular magnetic anisotropy of the CFO(111) thin film is $K_u = 2.09 \times 10^6\ \mathrm{erg/cm^3}$. The magneto-elastic effect theory reasonably explains the experimentally obtained PMA value. It suggests that the CFO(111) thin films required sufficiently large lattice stress and strain for stronger PMA. In addition to that, a barium hexaferrite (0001) thin film is also deposited on the sapphire substrate by using two different target compositions. The stoichiometric target gives Ba-rich BaM thin films and a Ba-rich target produces stoichiometric BaM thin films. Taking account of T-blocks into Ba-rich composition, the reductions of both saturation magnetization and magnetic anisotropy in the system were quantitatively explained.

The main objective of the present work was to prepare high-quality cobalt ferrite and barium hexaferrite thin films to be used as perpendicular magnetic recording media, successively used in a magneto-electric thin film heterostructure in low power device applications.

Chapter 1
Introduction

1.1 Duality of electric and magnetic field

The theme of wave-particle duality is at the core of most developments in physics [1]. Electromagnetic (EM) duality is founded on the idea that there is a considerable similarity between electricity and magnetism [2, 3]. The concept of EM duality was first proposed by Michael Faraday and made more precise with the formulation by James Clerk Maxwell of his famous equations of electric and magnetic fields [4-5]. The equations such as Gauss's law, Ampere's law and Faraday's law of induction were crucial for the advancement of electromagnetic devices [5-7].

$$\vec{\nabla}.\vec{B} = 0 \qquad (1.1)$$

$$\vec{\nabla}.\vec{E} = \vec{\rho}/\varepsilon \qquad (1.2)$$

$$\vec{\nabla} \times \vec{B} = \vec{j} + \varepsilon \frac{\overrightarrow{\partial E}}{\partial t} \qquad (1.3)$$

$$\vec{\nabla} \times \vec{E} = -\frac{\overrightarrow{\partial B}}{\partial t} \qquad (1.4)$$

Here $\vec{E}$ is the electric field, $\vec{B}$ the magnetic induction, ρ the density of electric charge, ε dielectric constant, and $\vec{j}$ the density of electric current.

Most magnetic devices such as magnetometers, motors, magnetic data storages device and electromagnets have electric current flowing through them. Stationary currents produce magnetic switching fields, whereby energy is converted to heat through resistive losses in the material (Joule heating effect). This energy loss is an irreversible process and contributes to the heating of other components in the device. Thus, the functionality and lifetime of the device decrease in due course of time.

1.1.1 Big data and importance of low power storage devices

The amount of data generated daily through the use of internet and smart-phones by industries, large organizations, research institutes and individuals is increasing at a very fast rate [8]. The storage of information from every sector, such as education, transportation, entertainment, health, business, environment, and so on, has already become an indispensable part of the many activities of human beings in the information era. Consequently, humans are entering an era of information explosion. It has been estimated that the information generated by the major sectors is nearly doubled each year [9]. According to a report prepared by the International Data Corporation (IDC)

in 2011, the total amount of data generated globally will reach 44 zettabytes (ZB) [1 ZB=10^{12} gigabytes (GB)] by 2020, as shown in Fig.1 [10]. The conventional way to store large amount of data is by using hard disk drives (HDD). The growth of HDD is likely to increase exponentially as compared to other storage devices. Shehabi *et al* wrote in, "a 2007 US Report that, the electricity use of the nation's servers and data centers in 2006 was more than double the electricity that was estimated to have been consumed for this purpose in 2000" [12]. As the number of HDD increases high energy power consumption and device related issues also increase. In order to reduce power consumption in storage facilities, an alternative way is the electric field control of magnetism.

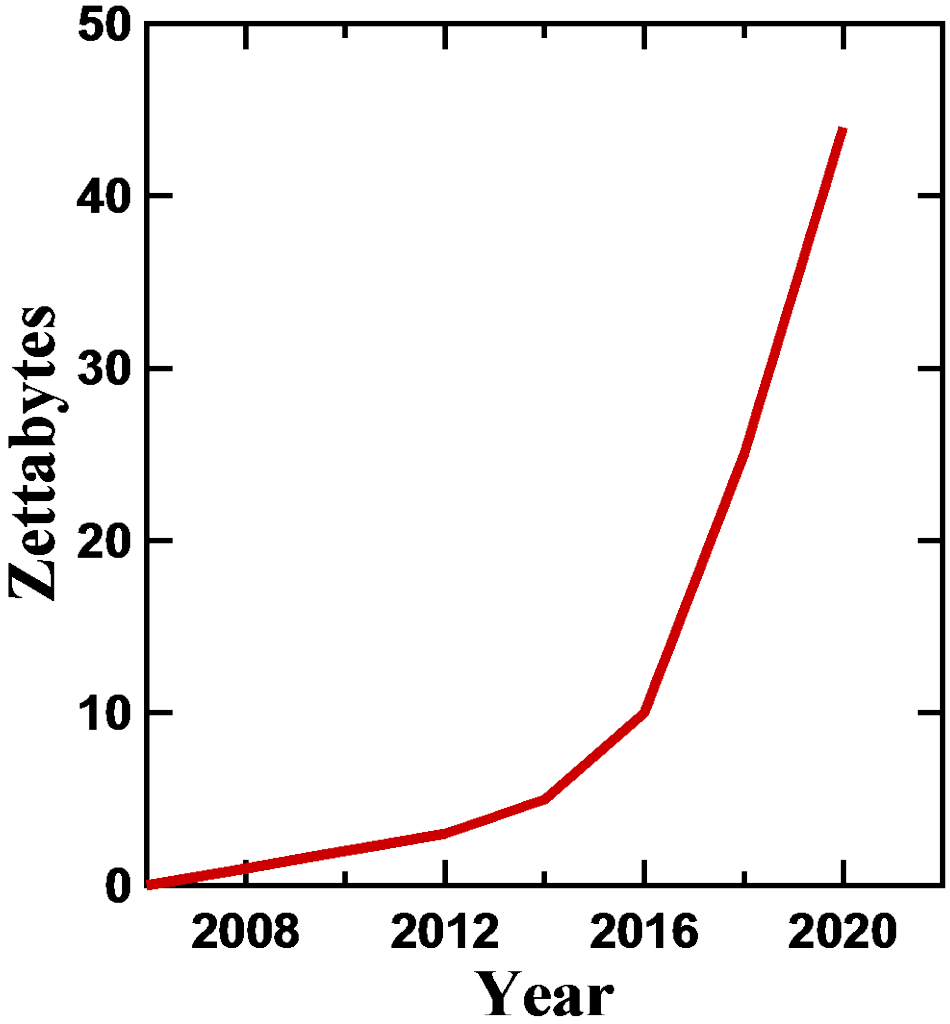

Fig. 1.1. Increasing trend of digital information [10]

1.2 Magneto-electric effect and Electric-field control of magnetism

1.2.1 Magneto-electric effect

Although the magneto-electric **(**ME) effect was predicted by Pierre Curie on the basis of crystal symmetry [13], the theoretical explanation by Landau and Lifshitz proved the feasibility of the ME effect in certain crystals [14]. Subsequently, the symmetry argument was applied by Dzyaloshinskii to antiferromagnetic Cr_2O_3 [15]. Astrov *et al* reported the experimental evidence of ME in Cr_2O_3 [16]. The ME effect was later observed in some single phase crystal families, e.g., perovskite-type $BiFeO_3$ [17, 18], $BiMnO_3$ [19], $TbMnO_3$ [20], and hexagonal (RE) MnO_3 (RE = rare earth) [21]. Note that most of these compounds displayed antiferromagnetic behavior.

Magnetoelectric films have been proposed as key components for electronic and magnetic applications. The magnetoelectric effect describes the induction of electric polarization by means of a magnetic field and magnetization by an electric field – providing another route for the linking of magnetic and electric properties [17, 22]. This relationship can be expressed by the following equations [16, 17, 22]:

$$\vec{P} = \epsilon\vec{E} + \alpha\vec{H} \qquad (1.5)$$

$$\vec{M} = \chi\vec{H} + \alpha\vec{E} \qquad (1.6)$$

Here, $\vec{M}$ is magnetization, $\vec{E}$ is electric field, $\vec{P}$ is polarization, $\vec{H}$ is magnetic field, ϵ is permittivity of the dielectric, χ is magnetic susceptibility and α is ME tensor.

The free energy of a material in an electric field $\vec{E}$ and/or a magnetic field $\vec{H}$ can be expanded as follows [89].

$$F(\vec{E},\vec{H}) = F_0 - P_i^s E_i - M_i^s H_i - \frac{1}{2}\epsilon_0\epsilon_i E_i E_j - \frac{1}{2}\mu_0\mu_{ij} H_i H_j - \alpha_{ij} E_i H_j - \frac{1}{2}\beta_{ijk} E_i H_j H_k - \frac{1}{2}\gamma_{ijk} H_i E_j E_k - \cdots \qquad (1.7)$$

Where ϵ is the permittivity, μ is the permeability, and α is a second rank tensor known as the magnetoelectric susceptibility tensor. This equation can be differentiated to give the electric polarization *P* and the magnetization *M* of the material (with the superscript S denoting spontaneous components):

$$P_i(\vec{E},\vec{H}) = -\frac{\partial F}{\partial E_i} = P_i^s + \epsilon_0\epsilon_{ij} E_j + \alpha_{ij} H_j + \frac{1}{2}\beta_{ijk} H_j H_k + \frac{1}{2}\gamma_{ijk} H_i E_j - \cdots \qquad (1.8)$$

$$M_i(\vec{E},\vec{H}) = -\frac{\partial F}{\partial H_i} = M_i^s + \mu_0\mu_{ij} H_j + \alpha_{ij} E_i + \frac{1}{2}\beta_{ijk} E_i H_j + \frac{1}{2}\gamma_{ijk} E_j E_k - \cdots \quad (1.9)$$

It can be seen from Equations 1.8 and 1.9 that α describes a cross-coupling between the electric polarization and magnetic field, and the magnetization and electric field, respectively. This coupling is the so-called linear magnetoelectric effect. The terms β and γ describe a higher order coupling. The magnetoelectric effect is expected to be large in ferroelectric and ferromagnetic materials [17, 23]. Two classes of multiferroics that display large magnetoelectric coupling are composites, where the magnetoelectric effect is the property of magnetostrictive and piezoelectric materials, as well as single phase multiferroics, where the magnetoelectric coupling is intrinsic [23, 24].

1.2.2 Exchange coupling between ferro-/ferri- magnetic and antiferromagnetic heterostructrues

In 1956 W. H. Meiklejohn *et al* reported a new type of magnetic anisotropy best described as exchange anisotropy. This anisotropy was the result of an interaction between an antiferromagnetic (AFM) material and a ferromagnetic (FM) material. The exchange anisotropy showed unidirectional characteristics, generating one easy direction of magnetization [25-26]. This effect was observed in samples with an antiferromagnetic/ferro- or ferrimagnetic (FMI) interface when they are cooled down in a magnetic field from above the Neel temperature, T_N, of the AFM. Exchange bias is induced showing a shift of the hysteresis loop along the magnetic field axis as shown in Fig. 1.2 [26]. This corresponds to the exchange coupling field (H_{ex}), which decreases with increasing temperature and disappears at the critical temperature known as the blocking temperature (T_B). The phenomenological formula of the exchange field is given by [27-28]

$$H_{ex} = \frac{2J_{ex}\, S(FM)\, S(AFM)}{a^2\, M(FM)\, t(FM)}$$

Here J_{ex} is the exchange parameter, S(FM) and S(AFM) are the spins of the interfacial atoms, t is the thickness of the FM film, M the magnetization of the FM layer, and *a* the lattice parameter.

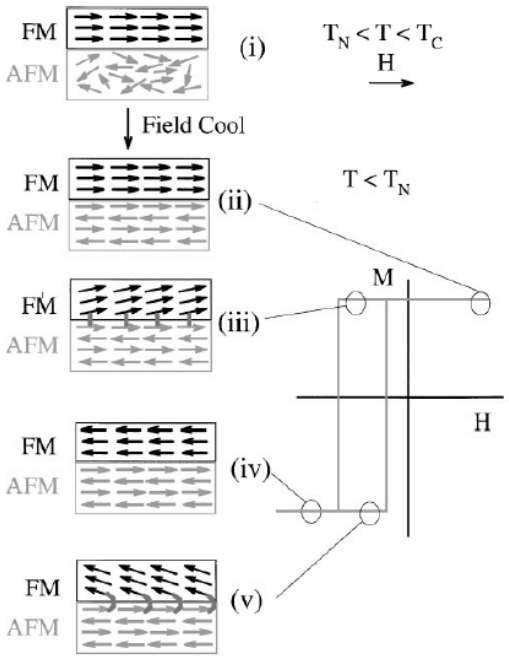

Fig. 1.2. Phenomenological model of exchange bias. (i) The high temperature spin configuration and magnetic response. Figures (ii-v) show the magnetic response and spin configurations at several points in the magnetic hysteresis curve, taken after cooling below the Neel temperature in a magnetic field [28].

1.2.2. (a) Exchange bias in thin films

Exchange bias materials, in a thin film form, have been widely studied [27-28]. In these systems, the interface can be quite effectively controlled and characterized. Among the layered systems, AFM-ferromagnetic [27-28] interfaces are most commonly investigated, however related systems such as AFM-ferrimagnetic [27-28] interfaces have also been studied.

1.2.2. (b) Antiferromagnetic-ferromagnetic interface structure

The distribution of blocking temperatures in the exchange coupled 40 nm $Ni_{81}Fe_{19}$ /50 nm NiO films showed a decrease in the blocking temperature due to interfacial disorder and fluctuation in the interfaces [29]. The NiFe deposited on NiO(111) shows H_c = 550 Oe , H_{ex} = 100 Oe, and isotropic, while NiFe deposited on NiO(100) showed lower values than those of NiO(111) because of a high degree of spin compensation despite the uncompensated nature of the NiO(111) plane[30]. The highly orientated $Ni_{80}Fe_{20}$/ $Fe_{50}Mn_{50}$ bilayer deposited on Cu(111), (110) and (100), showed that the (111) oriented layer system is promising on account of the uncompensated spins at the interface [31]. The NiO/Ni double layer films prepared at low temperature showed higher H_{ex} and H_c as compare to high temperature thin films, because of nonstoichiometric $NiO_{1+\delta}$ grains and large anisotropy originating from the Ni^{3+} ions [32]. In case of NiO/NiFe bilayer grown on different

substrates, it was suggested that the enhanced exchange field is due to the small grain size of NiO, not because of texture, roughness or change in composition [33].

1.2.2. (c) Antiferromagnetic-ferrimagnetic interface structure

Observation of exchange bias in the superlattice structure of 2.2 nm CoO/Fe_3O_4 (9 nm) is due to strong magnetic interaction between the AFM and thin films [34]. The [111] Fe_3O_4/CoO bilayer thin films grown on α-Al_2O_3(0001) substrate showed that the H_{ex} was much smaller than the calculated value by reason of the influence of strain at the interface [35]. Similarly [100] Fe_3O_4/CoO bilayer thin films grown on $SrTiO_3$ showed higher exchange bias value than that previously reported on [111] Fe_3O_4/CoO bilayer thin films [36]. This higher exchange bias in [100] Fe_3O_4/CoO bilayer thin film was due to the presence of perpendicular coupling between CoO and net Fe_3O_4 moments, consistent with the calculations of the H_{ex} field [37]. Further investigation of the [100] Fe_3O_4/NiO superlattice structure showed Neel ordering in the NiO layer and Verwey ordering in Fe_3O_4 [38]. Such magnetic ordering is helpful in understanding the exchange bias system [39]. In addition, the Fe_3O_4/NiO interface study using polarized neutron reflectometry shed some light on the magnetic differences in the Fe_3O_4 possibly induced as a result of domain formation in the ferromagnetic layer [40-41].

The overall findings about the AFM / (FM or FMI) magnetic structure provide information about the unidirectional anisotropy of the system, which can be controlled by the interface. Such an interface should have uncompensated spins in the AFM layer which can be influenced by various factors such as the roughness, and thickness of the FM or FMI layer and so on.

1.2.3 Magneto-electric coupling and heterostructures

Recently, magnetoelectric random access memory (MERAM) considered as a potential candidate for next generation nonvolatile memories [42-44]. The magnetic multilayer Cu/Co/Cu thin films show current-induced magnetic switching of domains caused by the spin switching effect [45]. The voltage-controlled MERAM is also a promising solution for low power consumption, high storage density and room temperature operation, all at the same time [46]. Moreover, the MERAM device has been experimentally demonstrated using Cr_2O_3 ME materials, which are strong candidates for such devices [47]. Another promising candidate is $BiFeO_3$ which can possibly use room temperature manipulation of magnetization by an electric field for ME memory [48]. Chu *et al* showed that the ferromagnetic CoFe deposited on $BiFeO_3$ films can be controlled by electric field

and is also thus useful for magnetoelectric device applications [49]. Use of multiferroic materials as composites is also present promising candidates for electric field switching because of the magnetoelectric coupling between two-phase systems, as shown in Fig.1.3 [24]. Many papers have reported using multiferroic layered materials such as $BaTiO_3$ and $CoFe_2O_4$ composite[50], Terfenol-d/PZT [51], Terfenol-d/PZT in polymer matrix [52], Terfenol-d in polymer matrix /PZT in polymer matrix [53], $LaSrMnO_3$/PZT[54], $NiFe_2O_4$/PZT[54], CoFe/PMN-PT (lead magnesium niobate-lead titanate)[55], $Ni_{80}Co_{20}$/(110)PZN-PT(lead zinc niobate-lead titanate)[56], FeGaB/(110) PZN-PT[57], FeGaB/(110)PMN-PT[58], Fe_3O_4/PZN-PT[59], $NiFe_2O_4$/(001)PMN-PT[60], Ni/(110)PMN-PT[61], CoPd/(110)PMN-PT[62], $La_{0.67}Ca_{0.33}MnO_3$/PMN-PT[63], Co/PMN-PT[64], Ni/$Pb(Zr_xTi_{1x})O_3$/PZT[65], $Fe_{0.93}Ge_{0.07}$/$BiScO_3$-$PbTiO_3$[66], $BaTiO_3$/$NiFe_2O_4$/$SrTiO_3$ [67], $BiFeO_3$/ $NiFe_2O_4$ [68], and CoFe/Metglas [69].

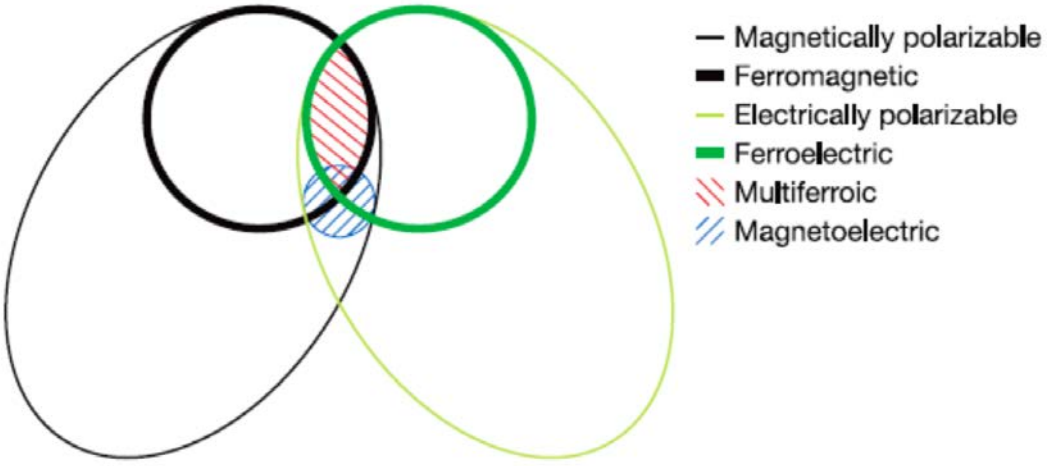

Fig. 1.3. Multiferroic materials with the coexistence of at least two ferroic properties [24]

1.2.4 Magneto-electric Cr_2O_3 and Electric-field control of magnetism

Magneto-electric materials are attractive candidates for non-volatile data storage because their magnetic and electric properties can be controlled by an external magnetic or electric field [47, 70-72]. One of the most promising is Cr_2O_3 because of its uncompensated spins parallel to the c–axis and the formation of ME domains [73]. The Neel temperature of Cr_2O_3 (anti-ferromagnetic material) is 307 K [74]. The net magnetic moment created by an electric field in a ME thin film influences the magnetization state of the neighboring ferromagnetic layer through exchange coupling [70]. Considering the application of the ME effect to storage/memory technology for voltage-controlled magnetization switching, there are many concerns including the above, which need to be resolved [47, 70-71, 75]. The first is to realize and design an effectually high exchange-

bias field between the Cr_2O_3 and FM thin film layers [71-72, 75-78]. The second issue is controlling the ferromagnetic metallic layer. The problem with the ferromagnetic metallic layer is single bit manipulation, which is not easy using electric field control. To overcome such problems, it is necessary to replace the metallic layer with an insulating ferromagnetic layer a promising candidate for such a layer is magnetic oxide.

1.3 Role of ferrimagnetic materials as storage media

Ferrimagnetic materials are typical magnetic oxides [17, 79]. The theory and experimental results presented by Louis Neel is the foundation of ferrimagnetism [80]. The ferrites include the entire family of Fe-containing oxides such as spinels (AFe_2O_4) [79, 81-83], garnets (AFe_5O_{12}) [84], hexaferrites ($AFe_{12}O_{19}$) [82, 85], (where A is a bivalent metal ion) and orthoferrites ($RFeO_3$, where R is one or more of the rare-earth elements) [86-87]. Among all of them Spinel ferrites and hexagonal ferrites materials show wide application potential by reason of their good insulating properties [88], high magnetic anisotropy [82], moderate saturation magnetization [83], high Curie temperature [83] and low microwave losses [79, 84-85]. The physical and magnetic properties of various ferrites are listed in table 1.1.

Table 1.1 Physical and magnetic properties of ferrites [81-88]

Compound	Crystal-type	Lattice constant (Å)	Magnetic Anisotropy K_1 (RT) (erg/cm^3)	M_s (RT) (emu/cm^3)	T_c (°C)	Resistivity (Ω . cm)
$CoFe_2O_4$	Spinel	a= 8.38	2.6×10^6	425	520	10^7
$BaFe_{12}O_{19}$	Magneto-plumbite	a=5.88 c=23.18	3.25×10^6	380	450	10^5
$Y_3Fe_5O_{12}$	Garnet	a=12.38	-0.61×10^4	140	286	10^{12}
$YFeO_3$	Perovskite	a=5.59 b=7.6 c=5.28	--	1.8	371	--

1.4 Previous reports on cobalt ferrite (111) and barium hexaferrite (0001) films

Cobalt ferrite (111) films

Previous reports on cobalt ferrite (111) films suggested that the easy axis of magnetization (out-of-plane) is hard to achieve and the obtained thin films in most cases seem to be isotropic [90-94]. The obtained saturation magnetization in the cobalt ferrite (111) thin films remained small (200-300

emu/cm^3) [90-94] as compared to the value in bulk cobalt ferrite (M_s = 425 emu/cm^3) as shown in Table 1.2 [83]. The cobalt ferrite (111) film reported in previous studies was thicker and the quality of the films suffered from deterioration [90-94].

Table 1.2 Previous reports on cobalt ferrite (111) films

Growth technique	Composition Co:Fe/Growth Temperature	Substrate	M_s (emu/cm^3)	K_u (Merg/cm^3)	References
PLD	1:2 550 ℃	Sc_2O_3(111)/ Si(111)	300 (10 K)	---	F. Sanchez et al 2011 (90)
PLD	1:2, 4:11 600 ℃	Pt(111)/SiO_2 /Si	250	---	M. Khodaei et al 2013 , 2014 (91 , 92)
PLD	1:2 450 ℃	α-Al_2O_3 (0001)	200	0.4	C. -W. Cho et al 2014 (93)
PLD	1:2 550 ℃	α-Al_2O_3 (0001) *Quartz	*300	2.5	J. H. Yin et al 2007 (94)

Barium hexaferrite (0001) films

Previous report on barium hexaferrite (0001) films suggested that the easy axis of saturation magnetization (out-of-plane) was small (200-366 emu/cm^3) [95-100] as compared to the value in bulk barium hexaferrite (M_s = 380 emu/cm^3) [83] as shown in Table 1.3.

Table 1.3 Previous reports on barium hexaferrite films

Growth technique	Growth temperature/ *Post annealing/ Thickness	Substrate	M_s (Out-of-plane) (emu/cm^3)	K_u (Merg/cm^3)	References
PLD	920 ℃ *1000 ℃ / 2h 500 nm	α-Al_2O_3 (0001)	366	---	S. R. Shinde et al 1998 (95)
PLD	900 ℃ 1600 nm	α-Al_2O_3 (0001)	334	---	S. A. Oliver et al 2000 (96)
PLD	800 ℃ / *950 ℃, 1000 ℃, 1050 ℃ 850 nm	Pt/MgO(111)	~318 ~302 ~200	---	H. Zheng et al 2016 (97)
RF Sputtering	*800 ℃ / 20 min. 90 nm - 150 nm	Si (100)	220	---	Z. Zhuang et al 1999 (98)
RF Sputtering	*750 ℃ / 5h 30 nm / 250 nm	α-Al_2O_3 (0001)	230/75	---	T. S. Cho et al 1999 (99)
MOCVD	800 ℃ 270 nm	Si/SiO_2 Al_2O_3 (0001)	292/ 307	1.32	S. Pignard et al 1999 (100)

The magnetic properties such as high magnetic anisotropy, saturation magnetization and good insulation of the CFO and BaM thin films suggested them to be possible candidates for

perpendicular magnetic recording (PMR) media. Determination of the preferred orientation of magnetization, perpendicular to the thin film by inducing stress with an appropriate α-Al_2O_3(0001) substrates. Thus, the goal of my research was to investigate perpendicular magnetic anisotropy (PMA) in the CFO(111) and BaM(0001) thin films using a substrate with trigonal symmetry, which can then be used ME thin film heterostructures .

1.5 Purpose of the study

This thesis investigates various structural, compositional, and magnetic properties of cobalt ferrite (111) and barium hexaferrite (0001) thin films. The epitaxial growth of cobalt ferrite (111) and barium hexaferrite (0001) thin films was performed by radio frequency magnetron sputtering. The main concern of this research work was to understand the easy axis of magnetization and magnetic anisotropy in the thin films. For the investigation of the physical and magnetic properties of the thin films different characterization techniques were used.

In brief, the motivation of my thesis is as follows:

1. Determination of the preferred orientation of magnetization, perpendicular to the thin film by inducing stress with an appropriate α-Al_2O_3(0001) substrates. The crystal field potential induced in the $CoFe_2O_4$ by uniform trigonal lattice deformation is only possible using a substrate with trigonal symmetry. In addition, the barium hexaferrite crystal system is the same as that of sapphire.
2. Optimization of the growth parameters such as growth temperature, composition ratio of target, sputtering chamber pressure, and post annealing temperature and time to control the preferred orientation of magnetic anisotropy in cobalt ferrite (111) and barium hexaferrite (0001) thin films.
3. To investigate perpendicular magnetic anisotropy in cobalt ferrite and barium hexaferrite thin films.

1.6 Outline of my thesis

Chapter 2 introduces the main experimental techniques. It includes description of the sample deposition techniques, and structural and magnetic characterization.

Chapter 3 presents the results of cobalt ferrite (111) thin films deposited on α-Al_2O_3(0001) substrates. Reactive radio frequency magnetron sputtering was found to be a useful technique for growing an epitaxial thin film of $Co_xFe_{3-x}O_4$ (CFO) (111). The magnetic properties of CFO(111)

thin films studies was investigated by optimizing the different conditional parameters such as growth temperature, oxygen flow rate, and thickness.

Chapter 4 presents the results on the barium hexaferrite (0001) thin films deposited on α-Al_2O_3(0001) substrates. The epitaxial growth of barium hexaferrite (0001) thin films was performed with two different target composition (stoichiometric: $BaFe_{12}O_{19}$, and barium-rich: $BaFe_{10}O_x$) by radio frequency magnetron sputtering. The study of barium hexaferrite (0001) thin films was carried out by optimizing the different conditions such as growth temperature, composition ratio of target, sputtering chamber pressure, and post annealing temperature and time.

Chapter 5 summarizes of the finding and also proposes some future works.

References

1. E. Castellani, European Philosophy of Science Association, (Springer 2009) pp.1-14.
2. P. A. M. Dirac, Proc. Roy. Soc. Lond. A, **133**, 60 (1931).
3. P. A. M. Dirac, Phys. Rev. **74**, 817 (1948).
4. P. Day, The Philosopher's Tree: Michael Faraday's life and work in his own words: A Selection of Michael Faraday's (1999).
5. D. J. Griffiths, Introduction to Electrodynamics (Pearson 4rd Edition, 2012).
6. R. P. Feynma, R. B. Leighton , M. Sands, The Feynman Lectures on Physics: Mainly Electromagnetism and Matter, Volume **2**, (Addison-Wesley, 1977) .
7. D. Halliday, R. Resnick, J. Walker, Fundamentals of Physics, (Wiley, 10th Edition , 2013).
8. R. Agrawal, C. Nyamful, Global journal of information technology, **6**, issue 1, 1 (2016).
9. M. Hilbert and P. Lopez, Science, **332,** 6025, 60 (2011).
10. https://www.emc.com/leadership/digital-universe/2014iview/executive-summary.htm.
11. http://www.martinhilbert.net/worldinfocapacity-html/.
12. A. Shehabi, S. Smith, D. Sartor, R. Brown, M. Herrlin, J. Koomey, E. Masanet, N. Horner, I. Azevedo, W. Lintner United States data center energy usage report, CA: Lawrence Berkeley National Laboratory. pp. 1-57, LBNL- 1005775 (2016).
13. P. Curie, J. Phys. Theor. Appl., **3**, 1, 393(1894).
14. L. D. Landau and E. M. Lifshitz, Electrodynamics of Continuous Media (Addison-Wesley, Reading, MA, 1960).
15. I. E. Dzyaloshinskii, J. Exptl. Theoret. Phys. (U.S.S.R.), **37**, 881(1959).
16. D. N. Astrov, J. Exptl. Theoret. Phys. (U.S.S.R.), **40**, 1035 (1961).
17. L. W. Martin, Y.-H. Chu, R. Ramesh, Mater. Sci. Eng**., R 68**, 89 (2010).
18. M. Fiebig, J. Phys. D, **38**, 8, R123 (2005).
19. F. Sugawara, J. Phys. Soc. Jpn., **20**, 1529 (1965).
20. M. Staruch, D. Violette, M. Jain, Mater. Chem. Phys., **139**, 2-3, 897(2013).
21. Q. H. Zhang, L. J. Wang, X. K. Wei, R. C. Yu, L. Gu, A. Hirata, M. W. Chen, C. Q. Jin, Y. Yao, Y. G. Wang, and X. F. Duan, Phys. Rev. B, **85**, 020102(R) (2012).
22. Y. Hao Chu, L. W. Martin, M. B. Holcomb, R, Ramesh, Mater. Today, **10**, 10, 16 (2007).
23. N. A. Spaldin, S.-Wook Cheong, and R. Ramesh, Phys. Today, **63**, 10, 38 (2010).
24. W. Eerenstein, N. D. Mathur, and J. F. Scott., Nature, **442**, 759 (2006).
25. W. H. Meiklejohn and C. P. Bean, Phys. Rev., **102**, 5 (1956).
26. W. H. Meiklejohn and C. P. Bean, Physical Rev., **105**, 3 (1957).

27. A. E. Berkowitz and K. Takano, J. Magn. Magn. Mater., **200**, 552 (1999).
28. J. Nogues and I. K. Schuller, J. Magn. Magn. Mater., **192**, 203 (1999).
29. S. Soeya, H. Hoshiya, and M. Fuyama, J. Appl. Phys., **76**, 5356 (1994).
30. C.-H. Lai**,** H. Matsuyama, R.L. White, IEEE Trans. Magn., **31**, 6, 2609 (1995).
31. R. Jungblut, R. Coehoorn, M. T. Johnson, Ch. Sauerb, P. J. van der Zaaga, A. R. Balla, Th. G. S. M. Rijks, J. aan de Stegge, A. Reinders, J. Magn. Magn. Mater., **148**, 1-2, 300 (1995).
32. K. Shimazawa, T. Baba, K. Kobayashi, K. Shinagawa, T. Saito and T. Tsushima, Jpn. J. Appl. Phys., **35**, L890 (1996).
33. C.-H. Lai**,** T. C. Anthony, E. Iwamura, R. L. White, IEEE Trans. Magn., **32**, 5, 3419 (1996).
34. T. Terashima, and Y. Bando, Thin Solid Films **152**, 3, 455 (1987).
35. P. J. van der Zaaga, R. M. Wolf, A. R. Ball, C. Bordel, L. F. Feiner, R. Jungblut, J. Magn. Magn. Mater., **148**, 1-2, 346 (1995).
36. P. J. van der Zaaga, A. R. Ball, L. F. Feiner, R. Jungblut, R. M. Wolf, P. A. A. van der Heijden, J. Appl. Phys.,**79**, 5103 (1996).
37. Y. Ijiri, A. Borchers, R. W. Erwin, S.-H. Lee, P. J. van der Zaag, and R. M. Wolf, Phys. Rev. Lett., **80**, 3, 608 (1998).
38. J. A. Borchers, R. W. Erwin, S. D. Berry, D. M. Lind, J. F. Ankner, E. Lochner, K. A. Shaw, and D. Hilton, Phys. Rev. B, **51**, 13, 8276 (1995).
39. D. M. Lind, S. D. Berry, J. A. Borchers, R. W. Erwin, E. Lochner, P. Stoyonov, K.A. Shaw, R. C. Dibari, J. Magn. Magn. Mater., **148**, 44(1995).
40. A. R. Ball, A. J. G. Leenaers, P. J. van der Zaag, K. A. Shaw, B. Singer, D. M. Lind, H. Fredrikze , M.Th. Rekveldt, Appl. Phys. Lett., **69**, 583(1996).
41. A. R. Ball, A. J. G. Leenaers, P. J. van der Zaag, K. A. Shaw, B. Singer, D. M. Lind, H. Fredrikze , M.Th. Rekveldt, Appl. Phys. Lett., **69**, 1489(1996).
42. G. A. Prinz, Science, **282,** 660 (1998).
43. J. M. Hu, Z. Li, L.Q. Chen, C. W. Nan, Nat. Commun. **2**, 553(2011).
44. J. Ma, J. M. Hu, Z. Li, C. W. Nan, Adv. Mater. **23**, 1062 (2011).
45. E. B. Myers, D. C. Ralph, J. A. Katine, R. N. Louie, R. A. Buhrman, Science, **285**, 867 (1999).
46. J. M. Hu, Z. Li, L. Q. Chen, C. W. Nan, Adv. Mater., **24**, 2869 (2012).
47. X. Chen, A. Hochstrat, P. Borisov, W. Kleemann, Appl. Phys. Lett., **89**, 202508 (2006).
48. M. Bibes, A. Barthélémy, Nat. Mater., **7**, 425 (2008).

49. Y.-H. Chu, L.W. Martin, M.B. Holcomb, M. Gajek, S.-J. Han, Q. He, N. Balke, C.-H. Yang, D. Lee, W. Hu, Q. Zhan, P.-L. Yang, A. Fraile-Rodríguez, A. Scholl, S.X. Wang, R. Ramesh, Nat. Mater., **7**, 478(2008).
50. A. M. D. G. Van Run, D. R. Terrell, D. H. Scholing, J. Mat. Sci., **9,** 1710 (1974).
51. J. Ryu, A. V. Carazo, K. Uchino and H.-E. Kim, Jpn. J. Appl. Phys, **40**, 4948 (2001).
52. C.-W. Nan, L. Liu, N. Cai, J. Zhai, Y. Ye, and Y. H. Lin, Appl. Phys. Lett. **81**, 3831 (2002).
53. N. Cai, C.-W. Nan, J. Zhai, and Y. Lin, Appl. Phys. Lett. **84**, 3516 (2004).
54. G. Srinivasan, E. T. Rasmussen, B. J. Levin, and R. Hayes, Phys. Rev. B, **65**, 134402 (2002).
55. T. L. Jin, L. Hao, J. W. Cao, M. F. Liu, H. G. Dang, Y. Wang, D. P. Wu, J. M. Bai, F. L. Wei, Appl. Phys. Express **7**, 043002 (2014).
56. M. Liu, S. D. Li, O. Obi, J. Lou, S. Rand, N. X. Sun, Appl. Phys. Lett., **98**, 222509(2011).
57. M. Liu, Z. Y. Zhou, T. X. Nan, B. M. Howe, G. J. Brown, N. X. Sun, Adv. Mater., **25**, 1435 (2013).
58. J. Lou, D. Reed, C. Pettiford, M. Liu, P. Han, S. Dong, N. X. Sun, Appl. Phys. Lett., **92**, 262502 (2008).
59. M. Liu, O. Obi, J. Lou, Y. J. Chen, Z. H. Cai, S. Stoute, M. Espanol, M. Lew, X. Situ, K. S. Ziemer, V. G. Harris, N. X. Sun, Adv. Funct. Mater., **19**, 1826 (2009).
60. J. H. Park, Y. K. Jeong, S. Ryu, J. Y. Son, H. M. Jang, Appl. Phys. Lett., **96**, 192504 (2010).
61. T. Wu, A. Bur, P. Zhao, K. P. Mohanchandra, K. Wong, K. L. Wang, C. S. Lynch, G. P. Carman, Appl. Phys. Lett., **98**, 262504 (2011).
62. J. H. Kim, K. S. Ryu, J. W. Jeong, S. C. Shin, Appl. Phys. Lett., **97**, 252508 (2010).
63. L. Wu, C. Zhang, C. Dong, C. Jia, C. Jiang, and D. Xue, Appl. Phys. Lett., **107**, 122905 (2015).
64. S. W. Yang, R.C. Peng, T. Jiang, Y. K. Liu, L. Feng, J. J. Wang, L. Q. Chen, X. G. Li, C. W. Nan, Adv. Mater., **26**, 7091(2014).
65. A. Brandlmaier, S. Geprägs, G. Woltersdorf, R. Gross, S. T. B. Goennenwein, J. Appl. Phys., **110**, 043913 (2011).
66. Z. Li, J. Wang, Y. Lin, C.W. Nan, Appl. Phys. Lett., **96,** 162505 (2010).
67. C. Deng, Y. Zhang, J. Ma, Y. Lin, C.-Wen Nan, Acta Mater., **56**, 3, 405(2008).
68. J. Gu, S. Yang, W. Yang, Y. Qi, G. Zhao, H. Sun, J. Magn. Magn. Mater., **349**, 140(2014).
69. W.-G. Yang, N. A. Morley, J. Sharp, and W. M. Rainforth, J. Appl. Phys. **118**, 034102 (2015).
70. R. Ramesh and N. A. Spaldin, Nat. Mater., **6**, 21(2007).
71. T. Ashida, Y. Sato, T. Nozaki, and M. Sahashi, J. Appl. Phys., **113**, 17D711 (2013).

72. T. Ashida, M. Oida, N. Shimomura, T. Nozaki, T. Shibata, and M. Sahashi, Appl. Phys. Lett. **104**, 152409 (2014).
73. P. J. Brown, J. B. Forsyth and F. Tasset, J. Phys.: Condens. Matter **10**, 663 (1998).
74. S. P. Pati, N. Shimomura, T. Nozaki, T. Shibata, and M. Sahashi, J. App. Phys., **117**, 17D137 (2015).
75. T. Ashida, M. Oida, N. Shimomura, T. Nozaki, T. Shibata, and M. Sahashi, Appl. Phys. Lett., **106**, 132407 (2015).
76. T. Nozaki, Y. Sato, T. Ashida, N. Shimomura and M. Sahashi, Appl. Phys. Express, **7**, 093006 (2014).
77. K. Toyoki, Y. Shiratsuchi, A. Kobane, S. Harimoto, S. Onoue, H. Nomura, and R. Nakatani, J. App. Phys., **117**, 17D902 (2015).
78. M. AL-Mahdawi, S. P. Pati, Y. Shiokawa, S. Ye, T. Nozaki, and M. Sahashi, Phys. Rev. B, **95**, 144423 (2017).
79. G. F. Dionne, Magnetic Oxide, (Springe, 2009), pp.151-197.
80. https://www.nobelprize.org/nobel_prizes/physics/laureates/1970/neel-lecture.html.
81. S. Chikazumi, Physics of Ferromagnetism (Wiley 1996), pp.197-220.
82. R. O. Handley, Modern Magnetic Materials, (Wiley, New York, 2000), pp.123-131, 192, 485-491.
83. B. D. Cullity and C. D. Graham, Introduction to Magnetic Materials (Wiley, New York, 2009) 2nd ed., pp.175-193.
84. D. D. Stancil, A. Prabhakar, Spin Wave (Springer 2009), pp.333-334.
85. R. C. Pullar, Prog. Mat. Sci. **57**, 1191(2012).
86. R. M. Bozorth, V. Kramer, and J. P. Remeika, Phys. Rev. **1**, 1 (1958).
87. R. L. White, J. Appl. Phys. **40**, 1061 (1969).
88. Alex Goldman, Modern Ferrite Technology, (Springer; 2006), 2nd edition, pp.38.
89. M. Fiebig**,** J. Phys. D: Appl. Phys., **38,** R123 (2005).
90. F. Sanchez, R. Bachelet, P. de Coux, B. Warot-Fonrose, V. Skumryev, L. Tarnawska, P. Zaumseil, T. Schroeder, and J. Fontcuberta, Appl. Phys. Lett., **99**, 211910 (2011).
91. M. Khodaei, S. A. S. Ebrahimi, Y. J. Park, J. M. Ok, J. S. Kim, J. Son, and S. Baik, J. Magn. Magn. Mater. **340**, 16 (2013).
92. M. Khodaei, S. A. S. Ebrahimi, Y. J. Park, S. H. Choi, C. G. Kim, J. Son, S. Baik, Thin Solid Films, **571**, 62 (2014).
93. C.-W. Cho, D. Y. Lee, J. S. Bae, and S. Park, J. Magn. Magn. Mater. **368**, 149 (2014).

94. J. H. Yin, J. Ding, B. H. Liu, J. B. Yi, X. S. Miao, and J. S. Chen, J. Appl. Phys., **101**, 09K509 (2007).
95. S. R. Shinde, R. Ramesh, S. E. Lofland, S. M. Bhagat, S. B. Ogale, R. P. Sharma, T. Venkatesan, Appl. Phys. Lett., **72**, 3443(1998).
96. S. A. Oliver, M. L. Chen, I. Kozulin, C. Vittoria, J. Magn. Magn. Mater., **213**, 326(2000).
97. H. Zheng, M. Han, L. Zheng, J. Deng, P. Zheng, Q. Wu, L. Deng, H. Qin, J. Magn. Magn. Mater., **413**, 25(2016).
98. Z. Zhuang, M. H. Kryder, R.M. White, and D. E. Laughlin, Mat. Res. Soc. Symp. Proc., **577**, 605 (1999).
99. T. S. Cho, S. J. Doh, J. H. Je, and D.Y. Noh, J. Appl. Phys., **86**, 1958 (1999).
100. S. Pignard, H. Vincent, J.P. Senateur, Thin Solid Films, **350**, 119(1999).

Chapter 2
Experiments and Characterization Technique

This chapter gives a detailed description of the experimental method adopted for the deposition of cobalt ferrite and barium hexaferrite thin films. It also discusses the techniques used for characterization of the surface, composition, structural, and magnetic properties.

2.1 Magnetron Sputtering

There are various techniques for the deposition of thin films on a substrate; one of the most widely used being sputtering. Sputtering is a process by which atoms are ejected from a solid target material as a result of the bombardment of the target by energetic particles [1]. By first creating gaseous plasma and then accelerating the ions from this plasma into the source material target, the source material is eroded by the arriving ions by energy transfer and is ejected in the form of inert materials, i.e., either individual atoms or clusters of atoms or molecules [2]. Specifically, Ar inert gases are introduced into the vacuum chamber; the cathode is applied to the target, while the anode is applied to the substrate, so that glow discharge occurs. The Ar atoms are ionized, and then the accelerated ions strike the target. The targeted material is ejected and is deposited on the substrate as a thin film.

There are various types of sputtering systems, depending on the different kinds of power supplies. The most common type of sputtering system uses direct current (DC) power supplies in which direct voltage is applied. In the radio frequency (RF) sputtering system, AC voltage is used and much higher sputtering power is applied [2]. According to sputtering power, the discharge properties should be different. As a result, the properties of the thin films, size of the substrate, description of the target and the sputter velocity is changed when the power is changed. When DC power is used, only metal can be deposited. Insulated targets cannot be used with DC power. When RF power is used, the deposition of not only metals but also oxides, metallic oxides, and nitrides become possible [3]. In our laboratory, we used the method of reactive RF magnetron sputtering.

The principle of RF magnetron sputtering is that behind the target permanent magnets are arranged so that a magnetic field can be generated using the electrical field perpendicular to the target. The magnets in this setup have a distinct purpose, i.e., the field they produce may influence the electrons for a higher duration in the plasma due to the effect of the Lorentz force [2]. The more efficient secondary electron cyclotron motion not only promotes the ionization of the inert gases but also makes the sputtering more efficient. The benefits of such a system is higher

sputtering rate at low pressure, reduced the charge buildup, avoidance of substrate heating, localization of plasma, and quality control [2-4]. In my studies, the reactive radio frequency (RF) magnetron sputtering was used to deposit the epitaxial CFO(111) thin films on single-crystal α-Al_2O_3(0001) substrates. The metallic alloy target CoFe (Co:Fe=1:3) with a diameter of 2 inches was used. Prior to deposition, the substrates were annealed under vacuum at the growth temperature (T_g) for 1 hr. The films were deposited at various T_g values of 300, 400, 500, 550, and 600 ℃. The RF power of the sputtering process was set at 100 W. For the investigation of the oxygen flow rate dependence, the following constant parameters were used: growth temperature of 600 ℃ and film thickness of 50 nm. The flow rate of argon was kept constant at 30 sccm and the oxygen flow rate was changed from 2 to 10 sccm; total pressure inside the sputtering chamber was maintained at 0.5-0.6 Pa. In the thickness dependence study, the flow rate of oxygen gas was kept at 9 sccm and a growth temperature of 600 ℃ with various thicknesses of 9, 18, 25, 32, and 46 nm. The total pressure inside the sputtering chamber was maintained at 0.6 Pa.

Epitaxial growth of barium hexaferrite (0001) thin films was performed with two different target composition (stoichiometric: $BaFe_{12}O_{19}$, and barium-rich: $BaFe_{10}O_x$) on an α-Al_2O_3 (0001) substrate via radio frequency (RF) magnetron sputtering. The flow rate of Ar was 10 sccm; total pressure inside the sputtering chamber was maintained at 0.4-0.5 Pa. The RF power of the stoichiometric and barium-rich target was set at 100 W and 50 W. Both BaM(0001) thin films were post-annealed in atmosphere at 1000 ℃ for 10 minutes.

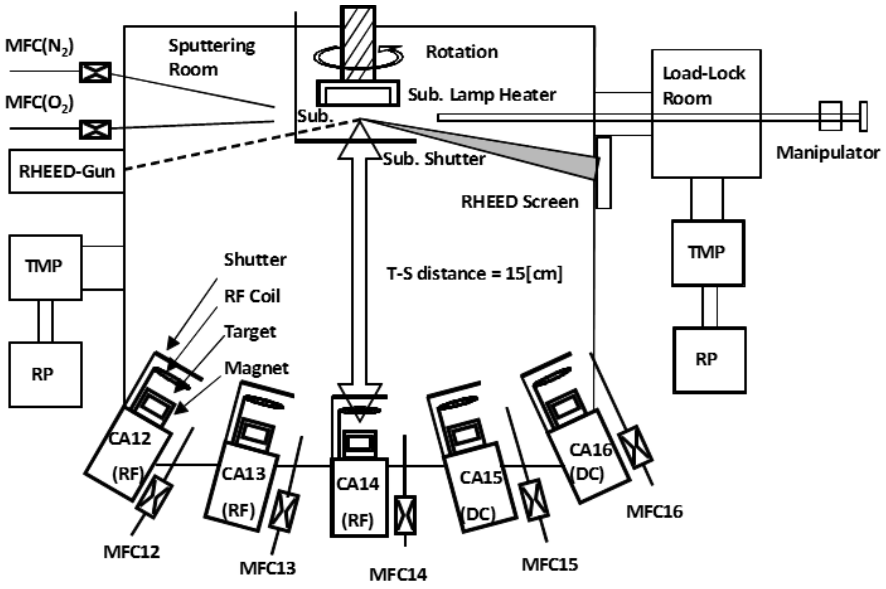

Fig. 2.1 A schematic diagram of the reactive RF magnetron sputtering system (MPS-6000, ULVAC) [5]

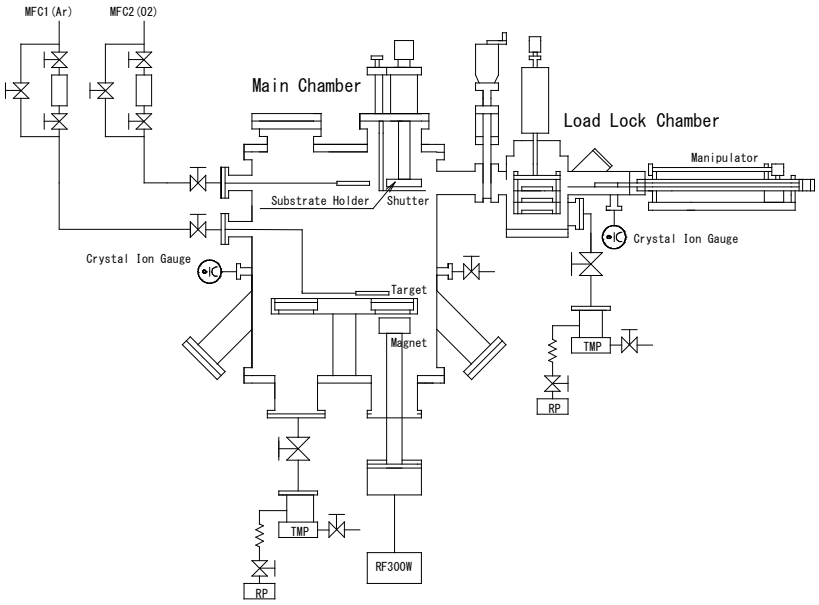

Fig. 2.2 A schematic diagram of the reactive RF magnetron sputtering system (Eiko ES-350SU) [6]

The reactive sputtering in an RF magnetron sputtering system (HV helicon magnetron sputtering system with five targets, ULVAC) was used for fabricating the cobalt ferrite and (EIKO ES-350SU) barium hexaferrite thin film samples in this study. Fig. 2.1 and 2.2 give the schematic diagrams of the sputtering system used for the deposition of the thin films.

2.2 Reflection High Energy Electron Diffraction (RHEED)

Reflection High Energy Electron Diffraction (RHEED) is one of the most common surface analytical tools used during physical vapor deposition [7].

An RHEED system requires an electron source (gun), detector, display screen and a sample with a clean surface. Figure 2.3 shows the basic set-up for an RHEED device, with the sample viewed edge-on. The electron gun causes a beam of electrons to strike the sample at a very small angle (2-6 degree) relative to the sample surface. Incident electrons diffract from atoms at the surface of the sample; the reflected beams are observed on a phosphor screen with a camera. The electron beam possesses accelerated energy of 20 keV to 30 keV, high enough to avoid the effect of electric and magnetic fields [8, 9].

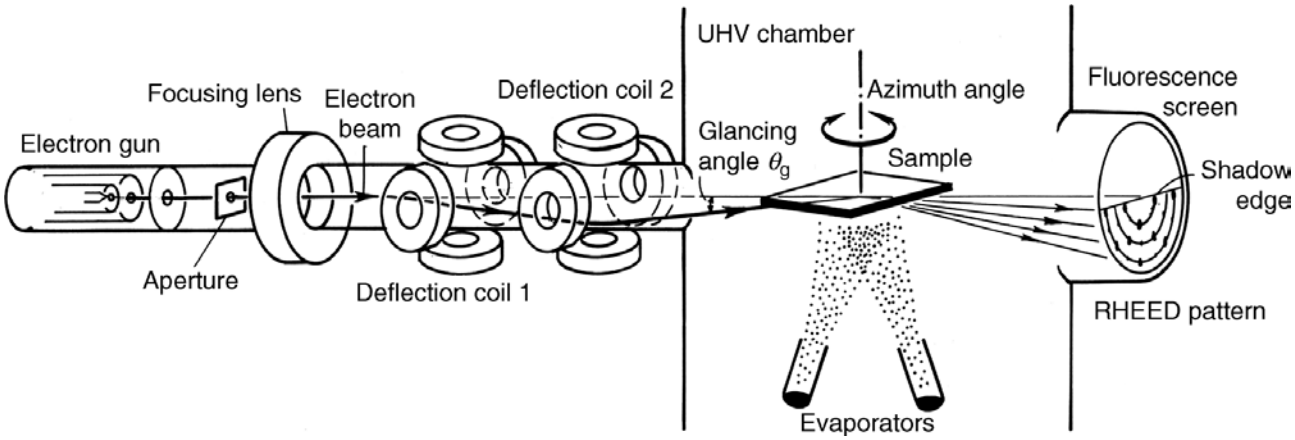

Fig. 2.3 A schematic illustration of RHEED apparatus [7]

The observed diffraction pattern is expressed by the reciprocal lattice space. The crystal structure can be analyzed from that pattern; the information of the flatness of the surface can be obtained from the shape of the diffraction spots [9]. When epitaxial thin film growth is achieved, RHEED would ideally produce a pattern with spots. But the ideal condition is not fulfilled in many cases on account of the density of atoms at the surface, and thus a streak pattern appears. If the surface is rough or textured, the diffraction pattern appears as a spot. In the case of polycrystalline thin film growth, the diffraction pattern appears as a ring. If the growth of materials is amorphous, the intensity of the diffracted beam is extremely weak, and no RHEED pattern appears. Figure 2.4 provides the information derived from RHEED pattern [10].

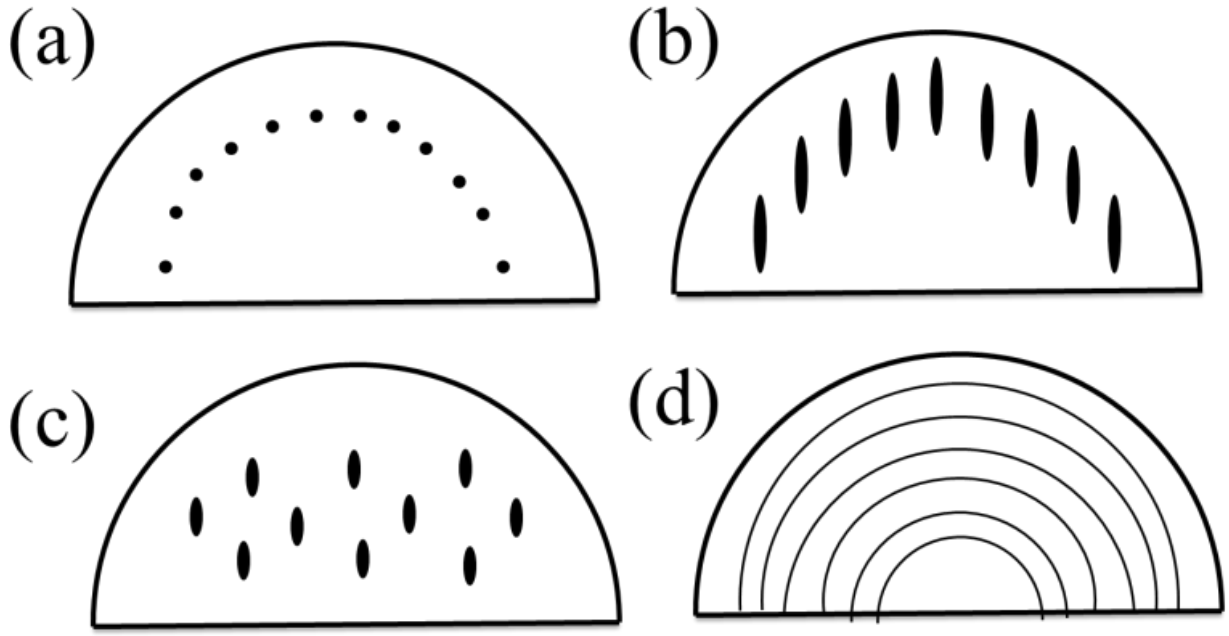

Fig. 2.4 An illustrations of RHEED pattern [10].

2.3 X-Ray Reflectivity (XRR)

X-ray reflectivity is the ratio of incident and reflected X-ray intensity. X-ray reflectivity gives information on the in-depth layered structure of the materials, such as layer thickness, layer density, and roughness of the surface and interfaces [11-12]. To measure the thickness of the thin films samples, with the method of X-Ray Reflectivity (XRR), an X-ray diffraction instrument (MINIFLEX, Riguku) was used. When the X-Ray is incident on a flat surface, three situations may occur depending on the different grazing angles [13-15]. Figure 2.5 indicates the X-ray optics for cases when the incident angle is smaller, equal to, and greater than the critical angle for the total reflection θ_c. When the incident angle is less than the total reflection critical angle, all incident X-rays are reflected. When the incident angle is equal to the total reflection critical angle, the incident X-rays propagate along the sample surface. When the incident angle is greater than the total reflection critical angle, the incident X-rays penetrate into the thin film by refraction. The oscillation interval is $\Delta 2\theta$, with given by Bragg's law [16], from which we can obtain the thickness of the sample.

$$2d \sin\left(\frac{\Delta 2\theta}{2}\right) = \lambda \qquad (2.1)$$

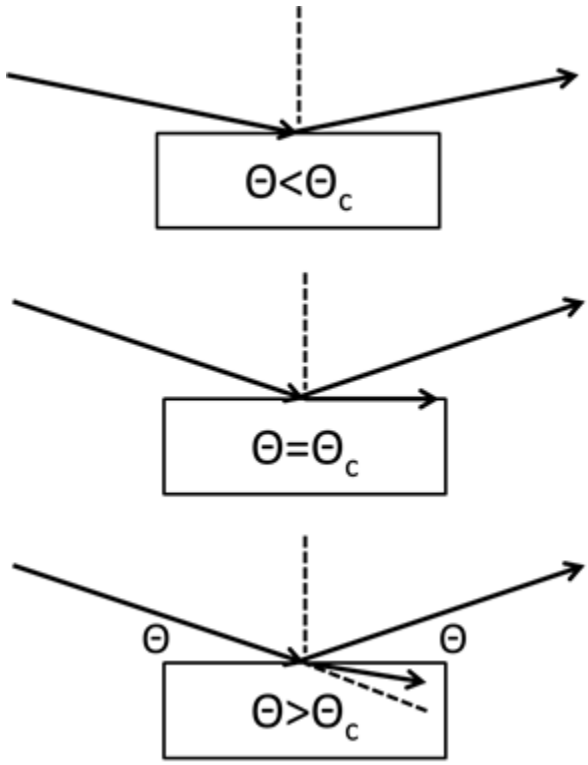

Fig. 2.5 Reflection, diffuse and refraction of X-rays at the surface of thin films with the changes of grazing angle [12].

Here λ is the X-ray wavelength. The source of radiation used in the experiment was the Cu Kα-

ray, with wavelength $\lambda = 1.5418$ Å. The applied voltage to the tube was 40 keV, and the current was 30 mA. The thickness measurement was done by using $\theta/2\theta$ scan.

2.4 X-ray Diffraction (XRD)

X-ray diffraction (XRD) is a dynamic nondestructive technique for characterizing crystalline materials [16]. It provides information on the crystal structure, phase, preferred crystal orientation (texture), and other structural parameters, such as average grain size, crystallinity, strain, and crystal defects [17]. X-ray diffraction peaks are produced by the constructive interference of a monochromatic beam of X-rays diffracted at determining angles from each set of lattice planes in a sample. The peak intensity depends on the distribution of atoms within the lattice. The X-ray diffraction pattern is thus the fingerprint of the periodic atomic arrangement in a given material [18]. The principle of X-ray diffraction is based on Bragg's law [16] as shown in Fig. 2.6. It, occurs when electromagnetic radiation or subatomic particle waves with wavelength comparable to the atomic spacing, are incident upon a crystalline sample, then scattered by the atoms in the system and undergo constructive interference.

Bragg's equation is given below [16]:

$$n\lambda = 2d \sin\theta \qquad (2.2)$$

Where n is an integer, λ is the wavelength, and θ is the angle of scattering.

The crystal structure and lattice distortions were analyzed by the X-ray diffraction (XRD) technique with Rigaku Smartlab based on the $\theta/2\theta$ (out-of-plane) and $2\theta_\chi$ (in-plane) angular scans, respectively. A Cu-Kα line was used as the X-ray source.

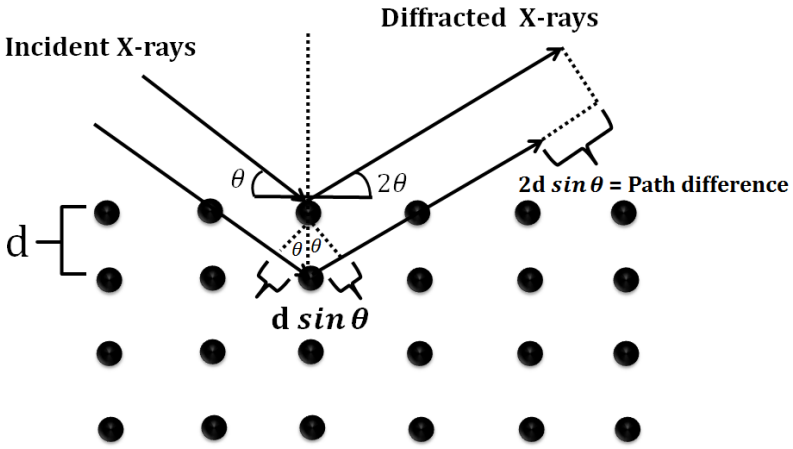

Fig. 2.6 Illustration of Bragg law [19]

2.5 Superconducting Quantum Interference Device—Vibrating Sample Magnetometer (SQUID-VSM)

The Vibrating Sample Magnetometer is an instrument that measures magnetic properties. A sample is placed inside a uniform magnetic field, and then sinusoidally vibrated [20]. An induced electromotive force is generated in the pickup coils. Superconducting Quantum Interference Device (SQUID) magnetometers can detect a change in an applied magnetics flux, and thus measure any physical observable that can be converted into magnetic flux, such as the magnetization of a sample. The measurement of the flux change through a pick-up coil system is based on the flux quantization within a superconducting loop [20-21]. The signal is proportional to the magnetic moment of a sample which is itself magnetized by the magnetic field produced by a superconducting magnet.

The SQUID-VSM is a combination of a SQUID and a VSM as shown in Fig. 2.7[21]. A superconducting magnet is used to apply magnetic field in the SQUID-VSM, which can be as large as ± 70 kOe. The speed of the magnetic field sweep is very high and it is quite good at temperature control during the measurement, as compared to the VSM.

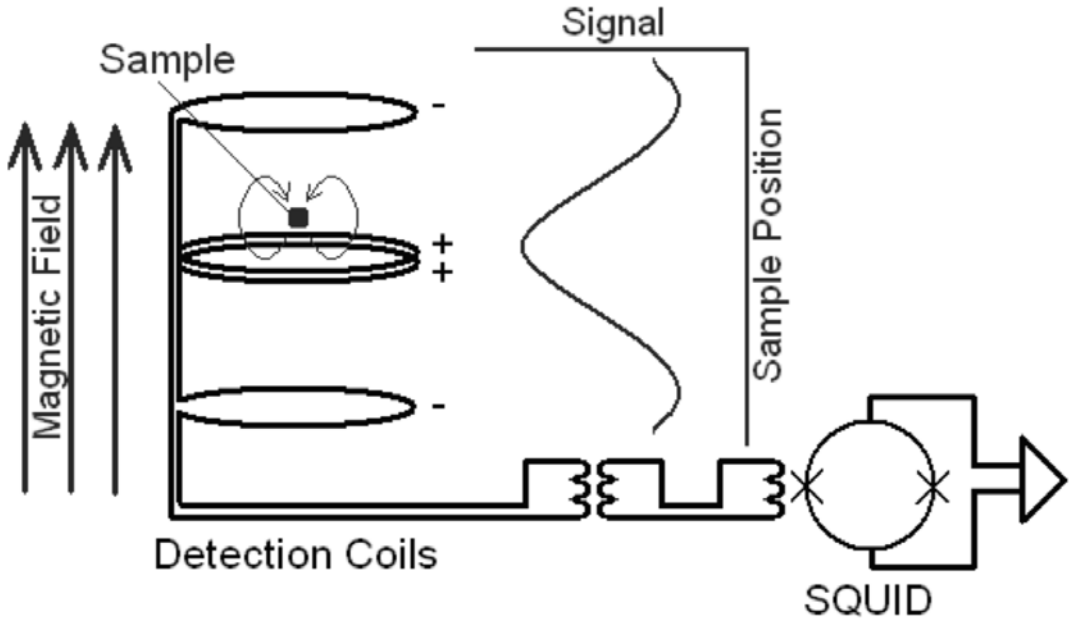

Fig. 2.7 SQUID-VSM detection schematic. (Quantum design MPMS) [21]

Principle

When two superconducting zones are kept isolated from each other, the phases of the electron-pairs in the two zones will be unrelated. If the two zones are brought closer together then some electron-pairs will become capable of tunneling across the gap, and the two electron-pair waves will become

coupled. The tunneling of the electron-pairs across the gap causes a superconducting current and is called “Josephson Tunneling”. The junction between the two superconductor is known the Josephson junction.

Let a superconductor with a gap have a critical current. If a supercurrent, i_s, flows across the gap between zones with a phase difference, $\Delta\emptyset$, it is related to the critical current, i_c, by [22]

$$i_s = i_c \sin \Delta\emptyset \qquad (2.3)$$

If the phase difference is $\frac{\pi}{2}$, then $i_s = i_c$ and hence, the maximum current flows across the gap.

Such properties can be useful in a Superconducting Quantum Interference Device (SQUID) for electron-pair wave coherence. Josephson junctions are also helpful in detecting very low magnetic fields. The central aspect of a SQUID is a ring of superconducting material with one or more weak links as is shown in Figure 2.8 [23]. This weak-links at points W and X have critical current, i_c, much lower than the critical current of the main ring. This generates a very low current density making the momentum of the electron-pairs small. Thus the wavelength of the electron-pairs becomes very long leading to little difference in phase between different parts of the ring.

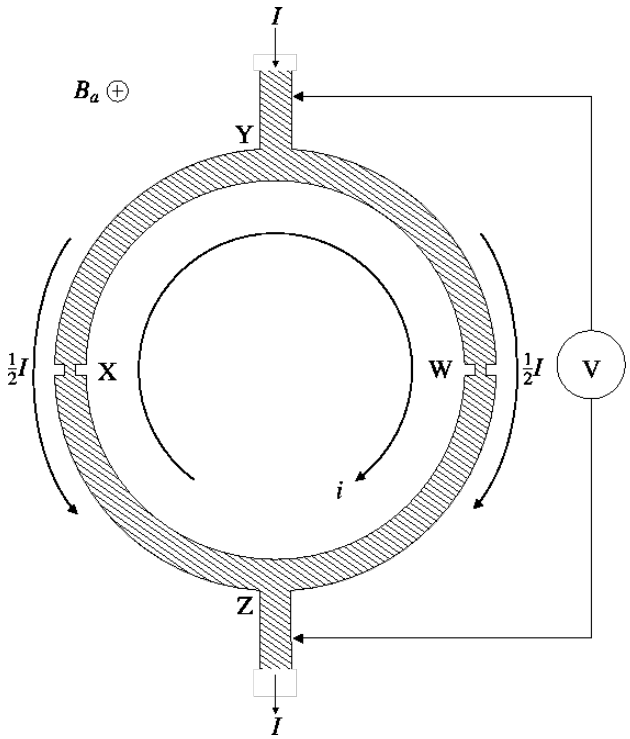

Fig. 2.8. Illustration of SQUID as a simple magnetometer [23]

If a magnetic field, B_a, is applied perpendicular to the plane of the ring, a phase difference is generated in the electron-pair wave along the path XYW and WZX. A low current, i, is also

induced to flow around the ring, producing a phase difference across the weak links. In addition to that, the induced current would be of an adequate extent to cancel the flux in the hole of the ring but the critical current of the weak-links prevents this.

The macroscopic quantum condition that the phase change around the closed path must equal $n2\pi$ can still be met by large phase differences across the weak-links produced by even a small current. An applied magnetic field produces a phase change around a ring, which in this case is equal to [23]

$$\Delta\emptyset(B) = 2\pi \frac{\Phi_a}{\Phi_0} \qquad (2.4)$$

Where Φ_a is the flux produced in the ring by the applied magnetic field. Φ_a may not necessarily equal an integral number of fluxons so to ensure the total phase change is a multiple of 2π a small current flows around the ring, generating a phase difference of $2\Delta\emptyset(i)$ across the two weak-links, giving a total phase change of [23]

$$\Delta\emptyset(B) + 2\Delta\emptyset(i) = n2\pi \qquad (2.5)$$

the phases difference due to the circulating current can either add to or subtract from that generated by the applied magnetic field but it is more energetically convenient to subtract: in this case a small anti-clockwise current, i^- [23].

Substituting values from Equations 2.4 and 2.5, the magnitude of the circulating current, i^-, can be obtained [23]

$$|i^-| = i_c \sin\pi \frac{\Phi_a}{\Phi_0} \qquad (2.6)$$

As the flux in the ring is enlarged from 0 to $1/2\ \Phi_0$ the magnitude of i^- increases to a maximum. As the flux is increased greater than $1/2\ \Phi_0$ it is now energetically favorable for a current, i^+, to flow in a clockwise direction, decreasing in magnitude to 0 as the flux reaches Φ_0. The circulating current has a periodic dependence on the magnitude of the applied field, with a period of variation of Φ_0, a very small amount of magnetic flux. Finding this circulating current enables the use of a SQUID as a magnetometer.

The circulating current generated by a flux change in the SQUID can be detected by the use of a measuring current, I. This current divides equally between both weak-links if the ring is symmetrical. While the current through the weak-links is small there will be no voltage detected across the ring. As I is increased it reaches a critical measuring current, I_c, at which voltages begin to be detected.

The significance of the critical measuring current is reliant upon the critical current of the weak-links and the limit of the phase transition around the ring being an integral multiple of 2π. For the integral ring to be superconducting the following condition must be met [24]

$$\alpha + \beta + 2\pi \frac{\Phi_a}{\Phi_0} = 2n\pi \qquad (2.7)$$

where α and β are the phase changes generated by currents across the weak-links and $2\pi \frac{\Phi_a}{\Phi_0}$ is the phase change due to the magnetic field.

When the measuring current is applied, α and β are no longer equal although their sum must remain constant. The phase changes can be written as [24]

$$\alpha = \pi \left[n - \left(\frac{\Phi_a}{\Phi_0}\right) \right] - \delta \qquad (2.8)$$

$$\beta = \pi \left[n - \left(\frac{\Phi_a}{\Phi_0}\right) \right] + \delta \qquad (2.9)$$

where δ is related to the measuring current I. Using the relation between current and phase in Equation 3.27 and rearranging to eliminate i we obtain an expression for I

$$I = 2i_c \left| \cos \pi \frac{\Phi_a}{\Phi_0} \, . \sin \delta \right| \qquad (2.10)$$

As $\sin \delta$ cannot be greater than unity, we can obtain the critical measuring current, I_c from Equation 2.10 as

$$I = 2i_c \left| \cos \pi \frac{\Phi_a}{\Phi_0} \right| \qquad (2.11)$$

This gives a repeated dependence on the magnitude of the magnetic field, with a maximum field, which gives us an integer number of fluxons and a minimum at half-integer values [24].

2.6 Torque Measurement

Magnetic anisotropy is a basic property of magnetic materials. The anisotropy can be intrinsic, related to atomic-scale interactions [25]. A torque magnetometer is widely used to measure magnetic moments and anisotropies [26]. The torque magnetometer technique consists basically in applying a magnetic field in a known direction relative to the sample and detecting the torque generated. If the sample is free to rotate, it will try to align its magnetization direction with the applied magnetic field direction. The torque is detected by measuring the restoring torque needed to

keep the sample in the original position. The torque magnetometer contains a sample holder, i.e. torque lever chip as shown in figure 2.9 [27].

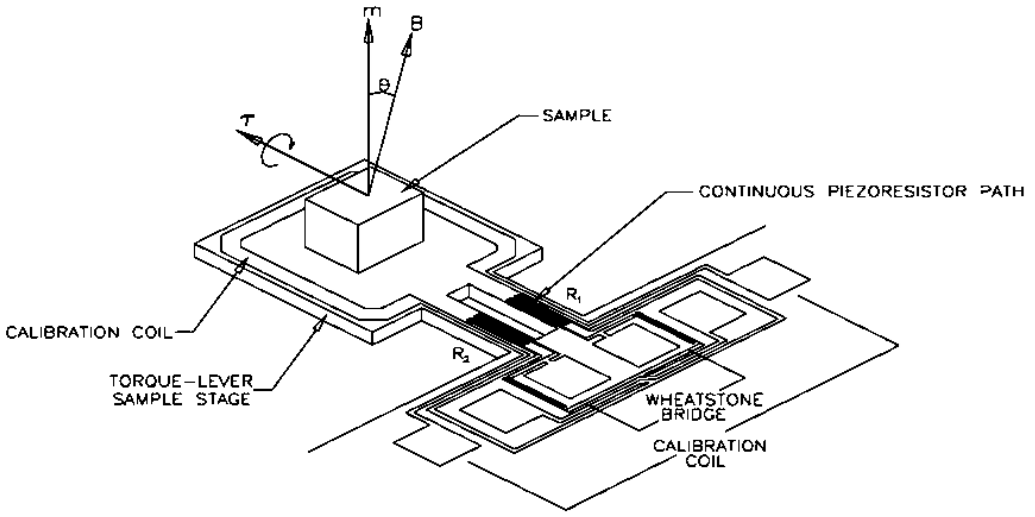

Fig. 2.9 A schematic illustration of torque measurement sample holder [27]

The torque can be determined by [26-27]:

$$\tau = m \times \mu_o H \qquad (2.12)$$

Here μ_o is the vacuum permeability; m is the magnetic moment of the restoring coil, related to the geometry (number of turns N and cross section A) and applied current (I) by the expression[26]:

$$m = NIAn \qquad (2.13)$$

n is a unit vector orthogonally aligned to the coils plane. The torque magnetometer sample holder uses a piezoresistive technique to measure the torsion, or twisting, of the torque lever about the lever's symmetry axis. These sample holders consist of a Wheatstone bridge circuit to measure to a high degree of sensitivity, the change in resistance, $\Delta(R_1 - R_2)$, of the piezoresistors grids [27]. By measuring the resistance, the user sample holder can accurately monitor the differential resistance in the piezoresistor grids. The differential resistance is caused by the magnetic torque.

2.7 Transmission Electron Microscopy (TEM)

A transmission electron microscope is a potent tool for material science as shown in figure 2.10 [28, 31]. A high energy beam of electrons is transmitted through a thin sample, and the interactions among the electrons and the atoms can be used to detect features in the crystal structure such as

dislocations and grain boundaries [28-29]. High resolution can be used to analyze the quality, shape, size, and defect [30]. The TEM operates on the principles of the light microscope but uses electrons instead of light. The wavelength of the electrons is much smaller than that of light. Because of this the resolution obtained for TEM images is much higher in magnitude than that of a light microscope. Therefore, TEM can reveal the important details of internal structure - in some cases in the range of individual atoms.

The TEM uses electromagnetic lenses to focus the electrons into a thin beam. The electron beam then travels through the sample. At the end of the microscope the unscattered electrons hit a fluorescent screen, giving rise to a "shadow image" of the sample with its different parts displayed in varied darkness depending on their density. The image formation can be studied directly by the operator or photographed with a camera.

The resolution of the TEM apparatus can be defined as:

$$r_d = 0.61\,\lambda/\alpha \qquad (2.14)$$

Where λ is the wavelength of the electrons (nanometers) and α is the angle between the converging radiation and the electron optic axis, (radians).

In practice, the resolution is limited by the spherical aberration, even where all other aberrations are negligible. As a result, the practical resolution r_{min} will be a combination of the limits imposed by the theoretical lens resolution and the spherical aberration:

$$r_{min} \sim 0.91\sqrt[4]{C_s\,\lambda^3} \quad (2.15)$$

The energy loss in the sample due to absorption introduces chromatic aberration, which cannot be ignored for thicker specimens where energy loss is appreciable. At 300 kV accelerating voltage, loss energy is more than 20 eV. The resolution then will be limited by the chromatic aberration term, or in other words the sample needs to be less than 50 nm thick to avoid chromatic aberration limited resolution.

Fig. 2.10 Image of TEM system (FEI Tecnai G^2 F30) [31]

2.8 Rutherford Backscattered Spectroscopy (RBS)

Rutherford backscattering spectroscopy (RBS) is used to determine the elemental composition ratio of the prepared sample. A target is bombarded with a helium ion beam with energy in the MeV-range, and the energy of the backscattered projectiles is recorded with a solid state detector [32-33]. RBS allows the quantitative analysis of the composition of a material and depth profiling of very small amount of elements. The RBS measurements of my samples were performed at the University of Tsukuba Tandem Accelerator Complex (UTTAC) with a 1 MeV high-resolution RBS system as shown in figure 2.11 [32, 34]. Table 2.1 provides in detail the parameters used while performing the RBS measurement.

Table 2.1 Parameter used during RBS measurement

Ion beam	**$^4He^+$**
Beam energy	**1.6 MeV**
Beam size (in diameter)	**1mm**
Beam current	**10 nA**
Scattering angle	**150°**
Incident angle	**0°**
Detector	**Solid state detector**
Sample type	**Thin film**

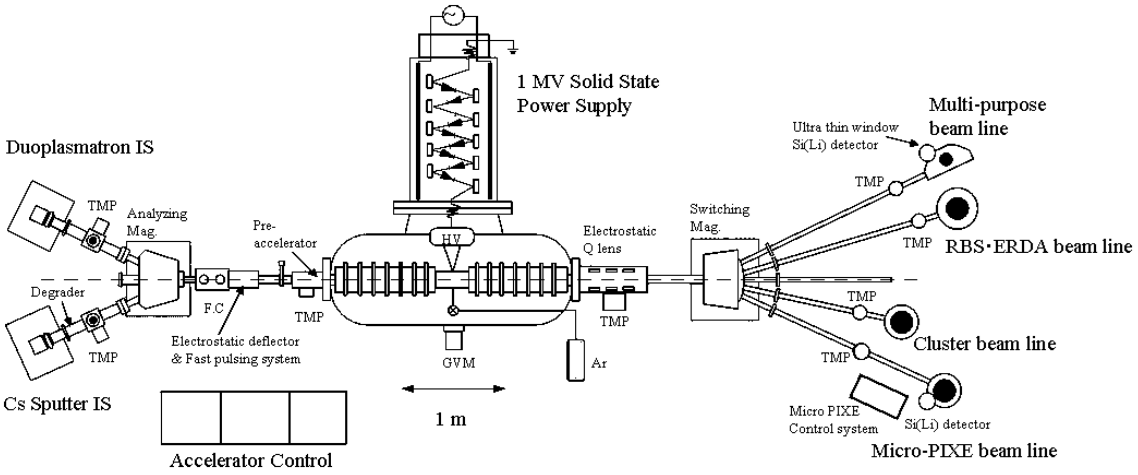

Fig. 2.11 A schematic illustrations of the RBS measurement system at UTTAC [32, 34]

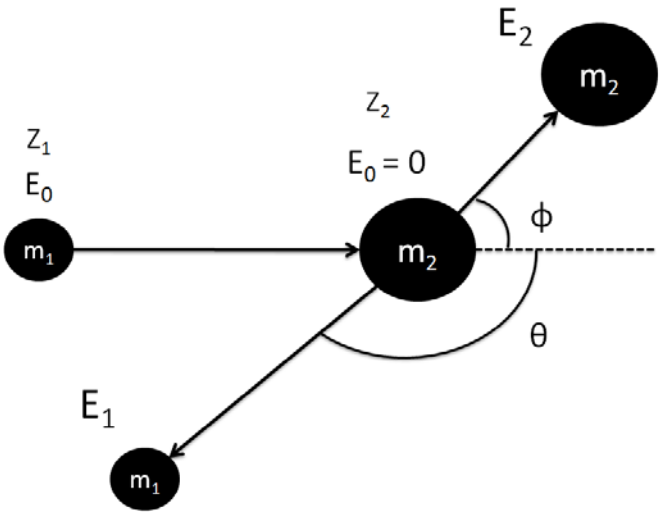

Fig. 2.12 A collision between two positively charged- particles. Before and after the collision, momentum and energy are conserved [35]

Basic principle

Kinematics

The main feature of RBS is its ability to identify the atomic masses of the elements present in the target. As shown in Figure 2.12., when helium ions collide with surface atoms, the energy of the ions after such an elastic scattering event is lower than its initial energy (E_0,) and the missing energy has been transferred to the recoiling target nuclei [35]. The ratio of the energy after and before the scattering event is known as the kinematic factor *K*.

Let us consider an ion of charge Z_1, mass m_1 and initial kinetic energy E_0 being scattered elastically from a stationary nucleus of charge Z_2 and mass m_2 purely by the Coulomb force. The final energy E_1 of the scattered ion is a function of the angle of scatter θ from the initial direction

Conservation of energy (elastic collision)

$$\frac{1}{2} m_1 v^2 = \frac{1}{2} m_1 v_1^2 + \frac{1}{2} m_2 v_2^2 \qquad (2.16)$$

Conservation of momentum

$$m_1 v = m_1 v_1 \cos\theta + m_2 v_2 \cos\emptyset \quad (2.17)$$

$$0 = m_1 v_1 \sin\theta - m_1 v_2 \sin\emptyset \qquad (2.18)$$

Eliminating $\emptyset$ using $\sin\emptyset + \cos\emptyset = 1$, the energy E_1 of a backscattered projectile with incident energy E_0 and mass m_1 after scattering is given by (in the laboratory frame of reference)[33, 35-37]

$$K = \frac{E_1}{E_0} = \left[\frac{\left(m_2^2 - m_1^2 \sin^2\theta\right)^{1/2} + m_1 \cos\theta}{m_2 + m_1}\right]^2 \qquad (2.19)$$

Rutherford Scattering Cross-section

As shown in fig. 2.13 the probability of scattered helium ions is given by the Rutherford cross sectional scattering formula [33, 36] i.e.

$$\frac{d\sigma}{d\Omega} = 5.18376 \times 10^6 \times \left(\frac{Z_1 Z_2}{E_0}\right)^2 \frac{\left\{\left(m_2^2 - m_1^2 \sin^2\theta\right)^{1/2} + m_1 \cos\theta\right\}^2}{m_2 \sin^4\theta \left(m_2^2 - m_1^2 \sin^2\theta\right)^{1/2}} \qquad (2.20)$$

Here the unit of the differential cross section is mb / sr (millibarns per steradian) when MeV is used as the unit for E_0.

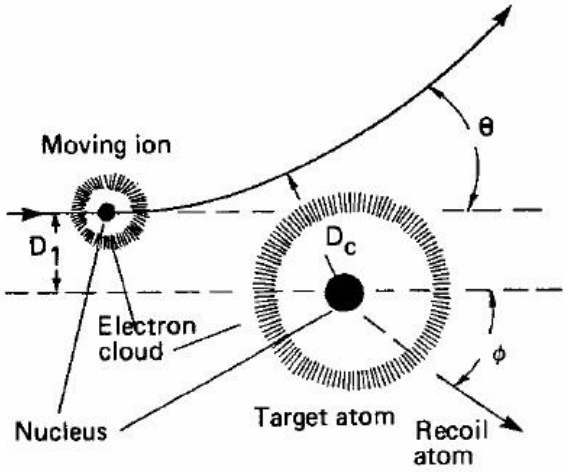

Fig. 2.13 A schematic illustration of Rutherford Cross Section [33, 35]

RBS spectra from thin and thick films calculated by using equation [35]:

$$A_i = (Nt)_i \times Q \times \Omega \times \frac{\sigma(E,\theta)}{\cos\theta} \quad (2.21)$$

where, A_i is the integrated peak count for each element on the surface, $(Nt)_i$ is density of atoms per unit area, Q is ion beam fluency [the number of incident particles (collected charge), measured by Faraday cup (Q= I x t)], Ω is solid angle of the detector , and $\frac{\sigma(E,\theta)}{\cos\theta}$ is the cross section of an element.

References

1. M. Ohring, The materials science of thin films. Boston: Academic Press (1992)
2. S. Swann, Magnetron sputtering, Phys. Technol. **19** (1988).
3. W. D. Westwood, Sputter deposition processes, MRS bulletin, December (1988).
4. D. Depla, S. Mahieu, J. E. Greene, Sputter deposition processes.
5. Radio Frequency (RF) sputtering system manual, MB1030, ULVAC (2012).
6. Y. Ikeda, Master Thesis, University of Tsukuba (2017).
7. S. Hasegawa, Characterization of materials, edited by Elton N. Kaufmann (John Wiley & Sons, 2012).
8. I. Bozovic and J. N. Eckstein, Analysis of growing films of complex oxides by RHEED MRS Bulletin, May (1995).
9. A. Ichimiya and P. I. Cohen, Reflection High Energy Electron Diffraction,(Cambridge University Press, 2004).
10. http://iramis.cea.fr/en/Phocea/Vie_des_labos/Ast/ast_sstechnique.php?id_ast=506.
11. P. Zaumseil, X-ray Reflectivity Characterization of Thin-Film and Multilayer Structures. In: Zschech E., Whelan C., Mikolajick T. (eds) Materials for Information Technology. Engineering Materials and Processes. (Springer, London 2005).
12. S. Kobayashi and K. Inaba, The Rigaku Journal, **28**, 1 (2012).
13. K. Sakurai, M. Mizusawa and M. Ishii, trans. Mater. Res. Japan, **33**, 3, 523(2008).
14. S. Kobayashi, The Rigaku Journal, **26**, 1 (2010).
15. L. G. Parratt, Phys. Rev., **95**, 2 (1954).
16. W. L. Bragg, Chapter 6, 50 Years of X-ray Diffraction edited by P. P. Ewald 1st ed. (1962) .
17. H. S. Kaufman and I. Frankuchen, Anal. Chem, **26**, 1, 31(1954).
18. A. A. Bunaciu, E. G. Udriştioiu and H. Y. Aboul-Enein, Critical Reviews in Analytical Chemistry, **45**, 4 (2015).
19. https://wiki.anton-paar.com/en/x-ray-diffraction-xrd/.
20. http://nptel.ac.in/syllabus/115103030/.
21. Quantum Design MPMS SQUID VSM User's Manual, Seventh edition, VSM Measurement Theory, part number 1500-100 C0, 4-2 (2009).
22. http://www.cmp.liv.ac.uk/frink/thesis/thesis/node46.html.
23. http://www.cmp.liv.ac.uk/frink/thesis/thesis/node47.html.
24. http://www.cmp.liv.ac.uk/frink/thesis/thesis/node48.html.
25. R. Andreescu, B. Spellman, E.P. Furlani, J. Magn. Magn. Mater. **320,** 1827 (2008).

26. J. Rigue, D. Chrischon, A. M. H de Andrade, M. Carara, J. Magn. Magn. Mater. **324**, 1561 (2012).
27. Quantum Design PPMS Torque magnetometer option User's Manual, third edition, VSM Measurement Theory, part number 1084-150 B, 1-1 & 1-2 (1999).
28. D. B. Williams, C. B. Carter, Transmission Electron Microscopy (Springer 2009) 2nd edition.
29. R. Gauvin, Proc. SPIE 10291, Materials Characterization and Optical Probe Techniques: A Critical Review, 102910C (1997).
30. H. Ma, K. Shieh, T. X. Qiao, Nature and Science, 4, 3, (2006).
31. http://www.nims.go.jp/tem/facility_seng_tecnai.html.
32. K. Sasa, S. Ishii, H. Oshima, Y. Tajima, T. Takahashi, Y. Yamato, D. Sekiba, T. Moriguchi, E.Kita , Proceedings of HIAT2015, THM2C02, Yokohama, Japan.
33. J. Perriere, Vacuum, **37**, 5, 429 (1987).
34. https://www.tac.tsukuba.ac.jp/uttac/tande.
35. http://www.physics.uwo.ca/~lgonchar/research/links/June3_2013/RBS_June3_2013_slides.pdf.
36. M. Mayer, Lectures given at the Workshop on Nuclear Data for Science and Technology: Materials Analysis Trieste, 19-30 May 2003.
37. http://nptel.ac.in/courses/115103030/

Chapter 3
Cobalt ferrite (111) thin films

3.1 Introduction

Spinel ferrites are ferromagnetic oxides [1] which crystallize with the same atomic structure as the magnetic mineral, $MgAl_2O_4$ [2]. Their chemical formula is $M^{2+}Fe^{3+}{}_2O_4$ where M = Mn^{2+} , Fe^{2+} , Co^{2+} , Ni^{2+} , Cu^{2+} , Zn^{2+} [1, 2]. The crystal structure of spinel ferrite is face centered cubic (FCC) within an oxygen framework. There are two types of spinel ferrites: normal spinel ferrites and inverse spinel ferrites. There are two distinct types of interstitial sites that the transition divalent metal ions occupy: tetrahedral (A) sites & octahedral (B) sites [3, 4]. If 8 M^{2+} ions occupy tetrahedral (A) sites and 16 Fe^{3+} ions occupy octahedral (B) sites, it is a normal spinel ferrite. On the other hand, if 8 Fe^{3+} ions occupy tetrahedral (A) sites and the octahedral (B) sites are occupied by 8 M^{2+} ions and 8 Fe^{3+} ions, it is termed an inverse spinel ferrite, as shown in Figure 3.1 [49]. The physical and magnetic properties of inverse spinel ferrite are listed in table 3.1 [3, 4].

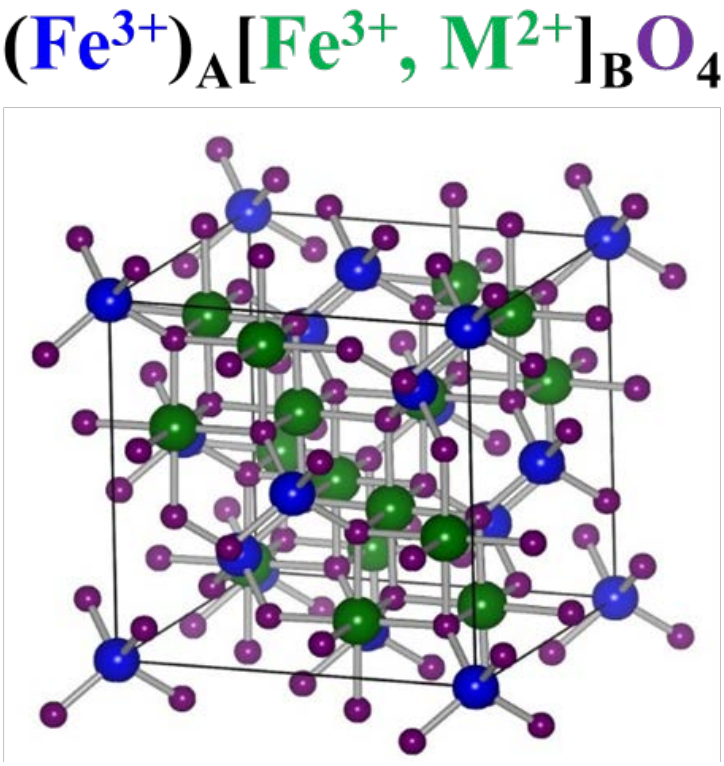

Fig. 3.1 Crystal structure of inverse spinel ferrite [49]

Table 3.1 Physical and magnetic properties of inverse spinel ferrite [3, 4]

Compound	Tetrahe-dral A (μ_B)	Octahe-dral B (μ_B)	Net (μ_B)	Lattice constant (Å)	Magnetic Anisotropy K_1 (RT) (erg/cm^3)	M_s (20 ℃) (emu/cm^3)	T_c (℃)
Fe_3O_4	5	5+4	4	8.39	-0.09×10^6	480	585
$MnFe_2O_4$	5	5+5	5	8.44	-0.03×10^6	400	300
$CoFe_2O_4$	5	5+3	3	8.38	2.6×10^6	425	520
$NiFe_2O_4$	5	5+2	2	8.34	-0.07×10^6	270	585

Cobalt ferrite

The cobalt ferrite is one of the most promising candidates among inverse spinel ferrites because of its moderate saturation magnetization (M_s), positive & strong magnetocrystalline anisotropy (K_1), and high Curie temperature (T_c) [3, 4]. This has generated interest for applications in spin filtering devices [5-8], multifunctional epitaxial heterostructures [9], and high-density magnetic recording media [10].

3.2 Magnetic anisotropy in cobalt ferrite

J. C. Slonczewski [11] proposed a single ion model for $Co_xFe_{3-x}O_4$, theoretically calculating the energy level in the transition metal ion by using crystal field theory. This theoretical model explained the large magnetic anisotropy of bulk cobalt ferrite [11]. In 1955 the magnetocrystalline anisotropy of $Co_{0.8}Fe_{2.2}O_4$ was found to be K_1 = 2.9 x 10^6 erg/cm^3 [12]. This experimental result could be successfully explained by the theoretical model [13]. Another theoretical study of cobalt ferrite thin films used the magneto-elastic theory [14]. Inoue *et al*. showed that if lattice distortion is introduced in a CFO thin film, the uniaxial anisotropy may be controlled through the orientation of the substrate and volume restriction [14]. Moreover, the extension theory using first principle calculations provided more information about the uniaxial magnetic anisotropy in the CFO thin film [15-16]. Hou *et al* showed that Co and Fe ions prefer high spin configurations with higher spin moments at the octahedral sites, no matter whether they were in a partial inverse spinel structure [17]. First principle calculations of magnetostriction of Fe_3O_4 and $CoFe_2O_4$ showed that the Co ions substituted in the octahedral Fe sites contributed to significant enhancement in the magnetostriction, of one order larger than that in Fe_3O_4 [18]. Moyer *et al* suggested that the Fe

doped cobalt ferrite thin film grown on MgO(001) showed an out-of-plane easy axis of magnetization, because of large Co^{2+} ion orbital moment [19]. Such a theoretical explanation suggests that the cobalt ferrite has very large magnetic anisotropy and large magnetostriction on account of the strong spin-orbit coupling of the Co^{2+} ion.

3.3 Lattice strain and magnetic anisotropy in cobalt ferrite thin film

Lattice strains appear to play a major role in influencing the differences in the magnetic behavior of cobalt ferrite thin films [20-38]. A strain-dependent uniaxial magnetic anisotropy (K_u) is consistently observed in $CoFe_2O_4$(001) thin films deposited on various substrates [20, 21].

The cobalt ferrite thin grown on MgO(001) and STO(001), showed tensile and compressive strain with an easy axis of magnetization perpendicular and parallel to the thin film [22]. It has been reported that $CoFe_2O_4$(111) epitaxial thin films grown on an Al_2O_3 substrate of 40 nm thickness show perpendicular magnetic anisotropy of 2.5 Merg/cm^3 with compressive stress in the film plane [23]. However, for thicker films of 200 nm thickness, a $CoFe_2O_4$(111) thin film grown on an α-Al_2O_3(0001) substrate by the pulse laser deposition (PLD) technique exhibits a preferential axis parallel to the film plane [24]. Khodaei *et al* reported that the $CoFe_2O_4$(111) thin films deposited on a Pt(111) buffer layer of 260 nm thickness exhibit in-plane magnetic anisotropy due to in-plane tensile stress [25]. Cobalt deficient, $Co_{0.8}Fe_{2.2}O_4$(111) films deposited on Pt buffer layer showed in-plane magnetization higher than that of $CoFe_2O_4$(111) thin films [26-27]. Moreover, the direction of the preferential axis of magnetization changed from out-of-plane to in-plane as the deposition temperature increases with the change in the sign of the lattice strain [28]. Yanagihara *et al* reported that the CFO(001) thin film grown by MBE showed lower magnetization, whereas the thin film grown by the sputtering method has higher magnetization comparable to the bulk CFO value of M_s = 425 emu/cm^3 [29, 30]. The CFO thin films deposited on STO(110) and (111) substrate, showed that after annealing, the magnetization of the (110) thin film increases, whereas the magnetization of the (111) thin film decreases due to the nano-growth twin structure [31]. Gatel *et al* showed an HRTEM image of CFO(100) and (111) grown on MAO with a large amount of interface dislocation in (111) thin films as compared to (100) [32]. Moreover, the CFO film on MgO(001) grown with different laser energy density of 0.2 J/cm^2 and 1 J/cm^2 showed PMA with lower energy density [33]. The optical bang gap of cobalt ferrite thin films deposited on Nb-doped STO showed indirect band gap of 1.42 eV owing to the defects present in the system [34]. Magnetic anisotropy changes if the SRO buffer layer is introduced in between the CFO/STO sample [35]. The heterostructure of CFO nanopillar embedded in a $BaTiO_3$ matrix showed magneto-electric coupling

[36]. Similarly, CFO thin film deposited on $BaTiO_3$ substrate also showed magneto-electric coupling [37]. Change in staking of the $BaTiO_3$ layer on to the top or bottom of the CFO layer strongly affects the magneto-electric coupling between them owing to the strain in the thin film at the interface [38].

The above contradictory results for cobalt ferrite (111) thin films suggest that its magnetic properties such as saturation magnetization, magnetic anisotropy, magnetization process, and so on are dependent on various parameters, which are in turn affected by the lattice strain. We studied the magnetic properties of $Co_xFe_{3-x}O_4$ (CFO) (111) thin films at different growth temperature (T_g), oxygen flow rate (O_2), and thickness (t) values. The purpose of this research was to understand the effect of lattice strain on the optimal growth conditions of CFO(111) thin films to achieve uniaxial magnetic anisotropy.

3.4 Experimental procedure

Epitaxial single-crystal thin films of CFO(111) with x=0.75 were grown on single-crystal α-Al_2O_3(0001) substrates with step-terrace treatment by reactive radio frequency (RF) magnetron sputtering. The metallic alloy target CoFe (Co:Fe=1:3) with a diameter of 2 in. was used. Prior to the deposition, the substrates were annealed under vacuum at the growth temperature for 1 hr. The films were deposited at various T_g values of 300, 400, 500, 550, and 600 ℃. The RF power of the sputtering process was set at 100 W.

For the investigation of the oxygen flow rate dependence, the following constant parameters were used: growth temperature of 600 ℃ and the film thickness of 50 nm. The flow rate of argon was kept constant at 30 sccm and the oxygen flow rate was changed from 2 to 10 sccm; total pressure inside the sputtering chamber was maintained at 0.5-0.6 Pa. In the thickness dependence study, the flow rate of oxygen gas was kept at 9 sccm and a growth temperature of 600 ℃ with various thicknesses of 9, 18, 25, 32, and 46 nm. The total pressure inside the sputtering chamber was maintained at 0.6 Pa.

3.5 Result and Discussion

3.5.1 Growth Temperature

The CFO thin films were grown at different growth temperatures of 300, 400, 500, 550, and 600 ℃. The typical RHEED patterns of the α-Al_2O_3(0001) substrate are shown in Fig. 3.2 (a-b). In Figs.

3.2 (c)-(g), the RHEED patterns taken after the deposition of the CFO thin films are shown. For the film grown at 300 ℃, the RHEED pattern shows rings indicating that the film is polycrystalline or textured. The films grown at temperatures greater than 500 ℃ are flat, but the RHEED streaks become significantly more diffuse with decreasing temperature, indicating reduced in-plane coherence due to the existence of inhomogeneous strains, the higher density of grain boundaries, and/or the increase in surface roughness. The sharp Kikuchi lines obtained from the CFO thin film provide evidence that epitaxial growth at higher temperatures leads to higher crystallinity.

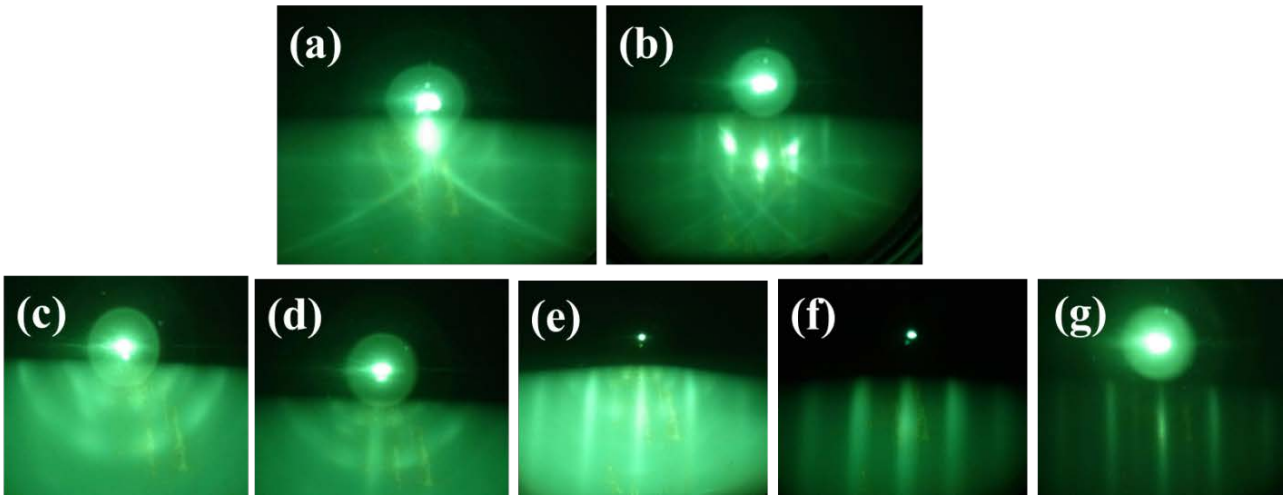

Fig. 3.2 (a-b) RHEED patterns along the directions based on the crystallographic axis of the α-Al_2O_3(0001) substrate. (c-g) RHEED patterns of CFO thin films grown at different growth temperatures (T_g) of 300, 400, 500, 550, and 600 ℃.

The XRD results of (symmetrical) $\theta/2\theta$ scans are shown in Fig. 3.3 for the CFO thin films grown on an α-Al_2O_3(0001) substrate at 300, 400, 500, 550, and 600 ℃ with an oxygen flow rate of 6 sccm and a thickness of 50 nm. These provide evidence of CFO formation, except for the pattern at 300 ℃. The epitaxial growth of CFO(111) thin films at growth temperatures higher than 400 ℃ was consistent with the RHEED patterns. At 300 ℃, no peak related to the spinel structure was detected, but a weak peak was observed at $2\theta \sim 45°$. Taking into account the ring patterns in the RHEED image, the film was found to be mainly composed of textured (Co, Fe)O_x(001) microcrystals rather than polycrystals.

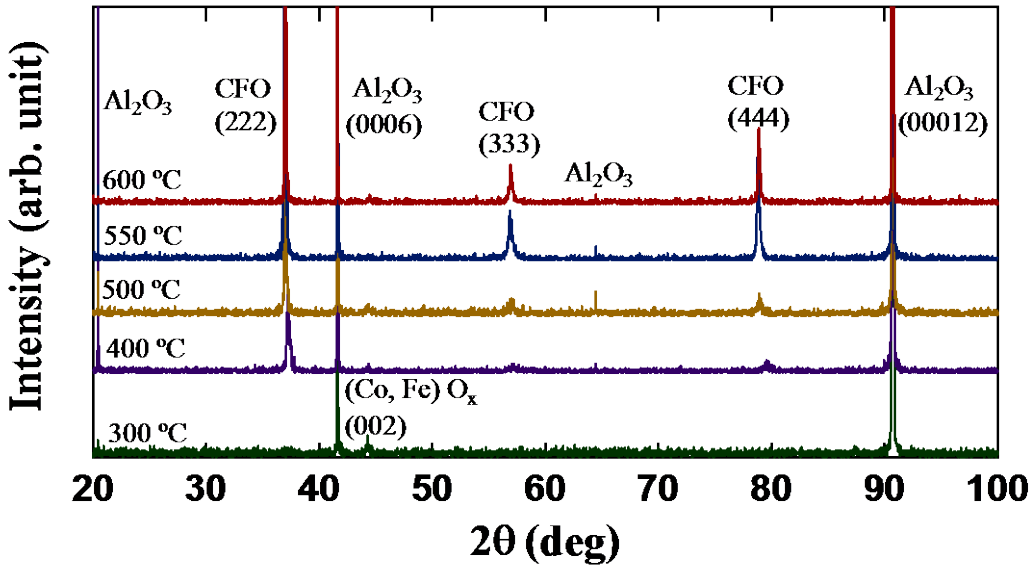

Fig. 3.3 Out-of-plane XRD θ/2θ scans of CFO(111) thin films grown on α-Al_2O_3(0001) substrate at 300, 400, 500, 550, and 600 ℃ with oxygen flow rate of 6 sccm and thickness of 50 nm.

The magnetic out-of-plane hysteresis loops of the CFO(111) thin films after subtracting the diamagnetic contribution of the substrate are presented in Fig. 3.4(a). The out-of-plane saturation magnetization (M_s) increases with increasing T_g and reaches 381 emu/cm^3 at T_g = 600 ℃. The observed M_s is slightly smaller than the bulk value of M_s = 425 emu/cm^3 [4]. According to the XRD results, the crystallinity improves with increasing growth temperature, resulting in an increase in M_s. The magnetic squareness ratio increases as the growth temperature increases. It was also found that the CFO(111) thin films grown at relatively low temperatures such as 300 and 400 ℃ exhibited a lower M_s than the bulk, suggesting that there are a number of structural imperfections, such as high-density antiphase boundaries (APBs) and secondary phase formations such as (Co, Fe)O_x. On the other hand, at 500, 550, and 600 ℃, the CFO(111) thin film seemed to saturate at a magnetic field of 60 kOe, quite a high magnetic field for saturation. This suggests that, at lower temperatures, a larger number of defects are responsible for the low magnetization, but at higher temperatures, the reduction in the number of defects improves the magnetic properties. Figure 3.4(b) shows that the saturation magnetization is larger at higher growth temperatures, close to the bulk value of $CoFe_2O_4$. This implies that the density of various defects is lower at higher temperatures and is similar to the previously reported APB behavior in Fe_3O_4(001) [39] thin films. The growth of single-crystalline thin films at higher temperatures is an advantageous growth condition for the CFO(111) thin film as it is accompanied by the reduction in the densities of surface and interfacial defects, which may arise at low temperatures [28].

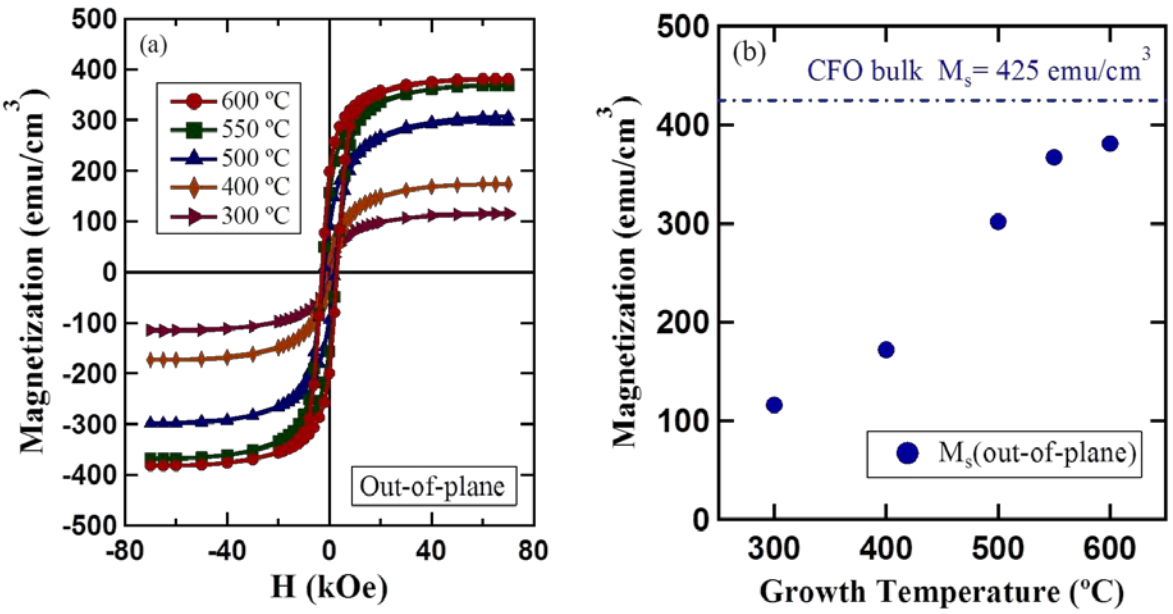

Fig. 3.4 (a) M-H loops (out-of-plane) of CFO(111) thin films with x=0.75 grown on α-Al_2O_3(0001) substrate at different temperatures with oxygen flow rate of 6 sccm and thickness of 50 nm. (b) the Plot of saturation magnetization (out-of-plane) vs. growth temperature of CFO thin films.

3.5.2 Oxygen gas flow rate

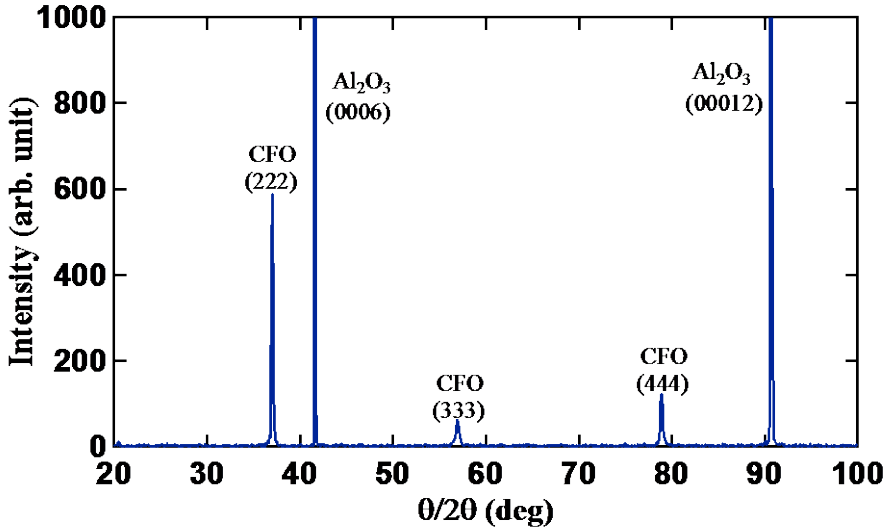

Fig. 3.5 Out-of-plane XRD θ/2θ scan of CFO(111) thin film grown on α-Al_2O_3(0001) substrate at 600 ℃ with oxygen flow rate of 9 sccm and thickness of 50 nm.

The XRD of the $\theta/2\theta$ scan is shown in Fig. 3.5 for the CFO thin films grown on the α-Al_2O_3(0001) substrate at 600 ℃ with an oxygen flow rate of 9 sccm and a thickness of 50 nm. The lattice strain

(ε) was defined as $(a\text{-}a_0)/a_0$, where a, 8.40 Å, is the lattice constant obtained from the peak positions (222), (333), and (444), while a_0, 8.39 Å, is obtained from the bulk lattice constant of $CoFe_2O_4$ [28, 40,41]. The very small lattice strain obtained from the average calculation was 0.11%, as expected.

Figure 3.6 shows the in-plane $2\theta_\chi/\phi$ scans used to determine the in-plane epitaxial relationship [42, 43]. The epitaxial relationship is CFO$[1\bar{1}0](111) \parallel$ α-$Al_2O_3[10\bar{1}0](0001)$. The lattice mismatch between CFO and α-Al_2O_3 is calculated as 8 % from the bulk values of the interplanar spacing of $d_{CFO\ (440)} = a/4\sqrt{2}$ Å [a=8.391 Å (ICDD No. 00-022-1086)] and $d_{\alpha-Al_2O_3\ (30\bar{3}0)} = a/2\sqrt{3}$ Å [a = 4.758 Å (ICDD No. 00-046-1212)]. An epitaxial relationship was previously reported [44]. Since the lattice mismatch is large between the thin film and the substrate, it is expected that the epitaxial strain will be promptly released at/or near the substrate/film interface [32, 45] and therefore incoherent epitaxial growth will occur.

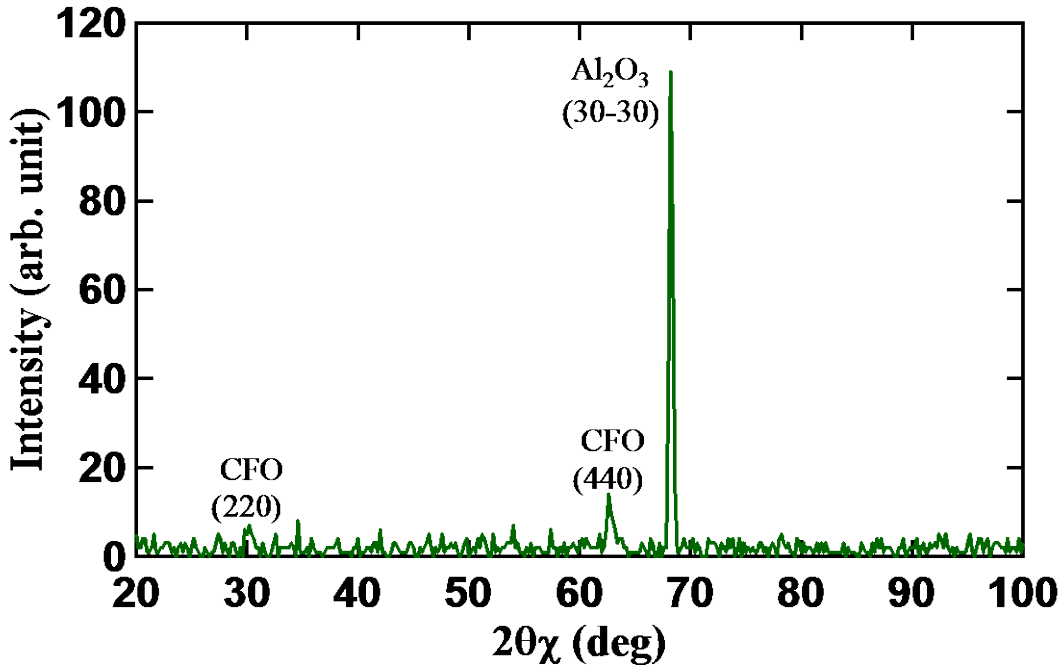

Fig. 3.6 In-plane XRD 2θχ scan of CFO(111) thin film grown on α-Al_2O_3(0001) substrate at 600 ℃ with oxygen flow rate of 9 sccm and thickness of 50 nm.

Oxygen flow rate also significantly affects the magnetic properties of CFO(111) films. The M-H loops of the CFO(111) thin film grown with an oxygen flow rate of 2-10 sccm at 600 ℃ measured in both in-plane and out-of-plane geometries at room temperature are shown in Fig. 3.7(a-i). The saturation magnetization of the CFO(111) film was 425 emu/cm^3, equal to the bulk value of $CoFe_2O_4$ (425 emu/cm^3) [4] at 8 sccm. Among the films grown at oxygen flow rates from 5 to 2

sccm, we observed a decrease in magnetization, although the XRD and RHEED patterns were similar to those of the films grown at higher oxygen flow rates.

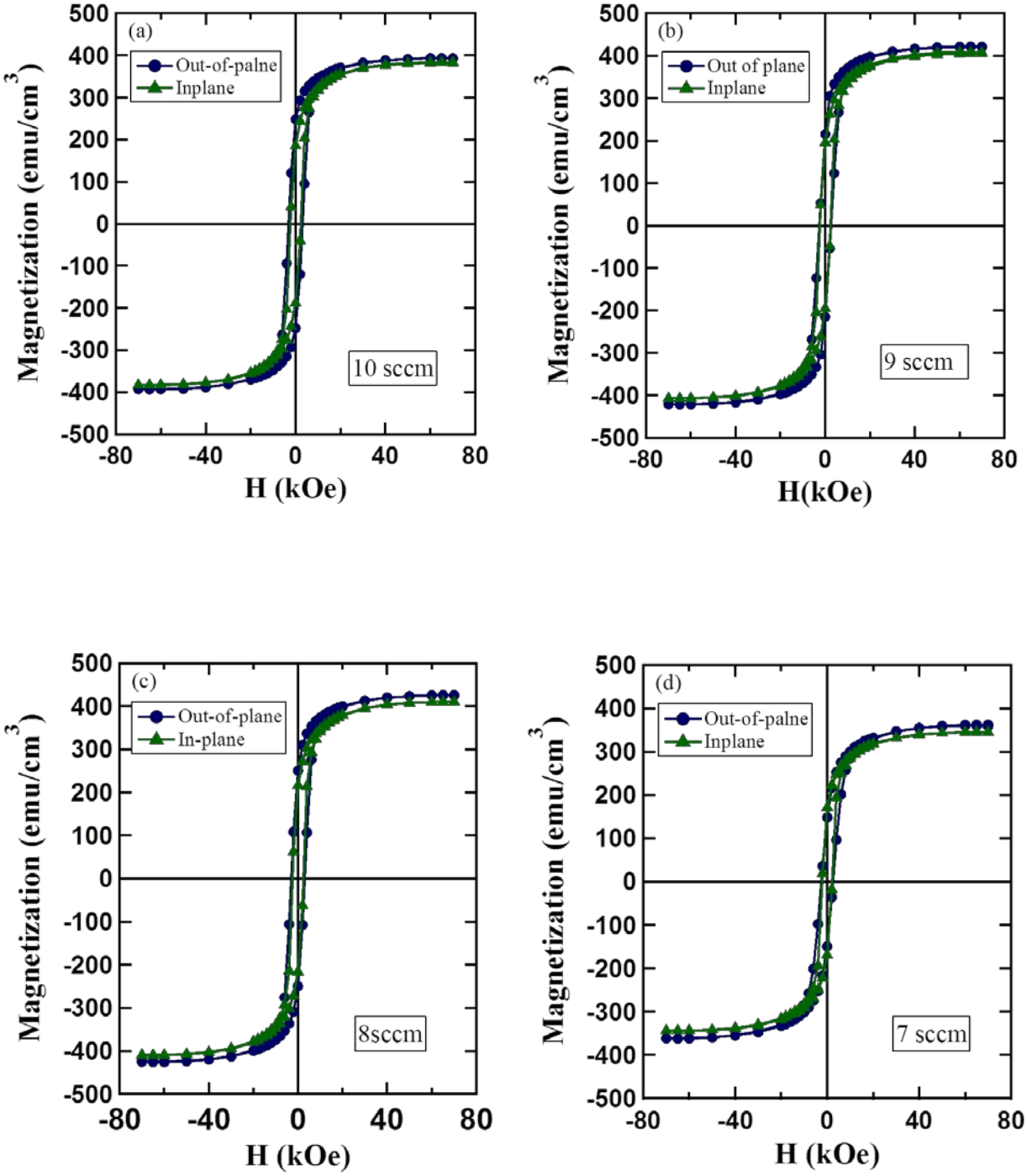

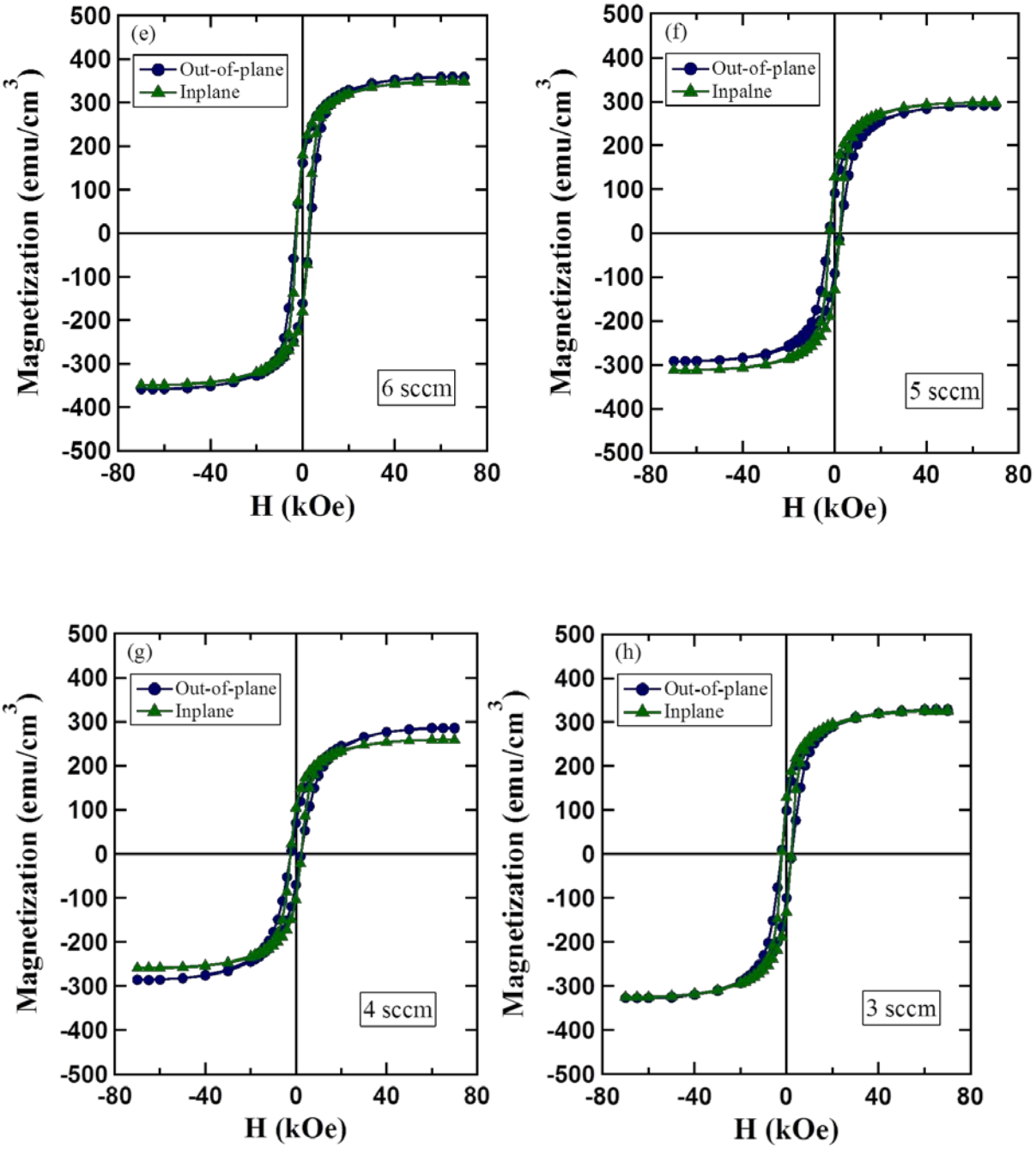
(e)
Out-of-plane
Inplane
6 sccm
(f)
Out-of-plane
Inpalne
5 sccm
(g)
Out-of-plane
Inplane
4 sccm
(h)
Out-of-plane
Inplane
3 sccm
Magnetization (emu/cm 3)
H (kOe)

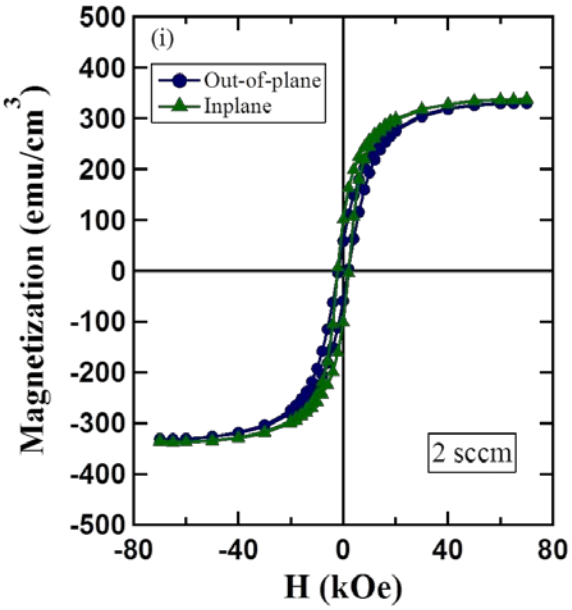

Fig. 3.7 (a-i) M-H loops of CFO(111) thin films grown on α-Al_2O_3(0001) substrate at 600 ℃ with oxygen flow rate of 10-2 sccm and thickness of 50 nm.

The torque measurement results for CFO(111) thin films at a field of 90 kOe with different oxygen flow rate of 10-2 sccm are shown in Fig. 3.8(a-b). The uniaxial magnetic anisotropy energy can be written as $E = K_u^{eff} \sin^2\theta$ [3, 4], where K_u^{eff} and θ are effective uniaxial magnetic anisotropy constant and the angle between saturation magnetization M_s and the easy axis, respectively. The intrinsic K_u is estimated by using the relation $K_u = K_u^{eff} + 2\pi M_s^2$. Here, the magnetic anisotropy energy is measured normal to the film plane. The uniaxial magnetic anisotropy of the CFO(111) thin film at an O_2 flow rate of 8 sccm is $K_u = 1.72 \times 10^6$ erg/cm^3, which is slightly lower than those at O_2 flow rates of 9 and 10 sccm. The uniaxial magnetic anisotropy of the CFO(111) thin film at an O_2 flow rate of 9 sccm is $K_u = 2.09 \times 10^6$ erg/cm^3, which is slightly small as compared to that of CFO(111)//Al_2O_3(0001) of $K_u = 2.5 \times 10^6$ erg/cm^3 [23]. The negative uniaxial magnetic anisotropy is observed with the decrease in the oxygen flow rate from 5 to 2 sccm.

The saturation magnetization (M_s) and effective uniaxial magnetic anisotropy (K_u^{eff}) values of CFO(111) thin films for different oxygen flow rates are shown in Fig.3.9. The slightly positive K_u can be understood by considering the magnetoelastic effect and the experimental results of lattice strain [46, 47]. Assuming equal volume transformation, the stress-induced magnetic anisotropy (K_σ) can be estimated as [23]

$$K_\sigma = \left(\frac{3}{2}\right)\lambda_{111}\ \sigma,$$

where $\lambda_{111} = 120 \times 10^{-6}$ [12] and σ indicate the stress. σ is related to the strain with $\sigma = Y_{111}\ \varepsilon$, where Y_{111} and ε are Young's modulus along <111> and the strain, respectively. For CFO, $Y_{111} = 9.29 \times 10^{12}$ dyne/cm^2 [23] and $\varepsilon = 0.0011$ as determined from

$$K_\sigma = 1.83 \times 10^6 \text{ erg/cm}^3 .$$

As shown here, both the estimated K_σ and experimentally obtained K_u are reasonably comparable.

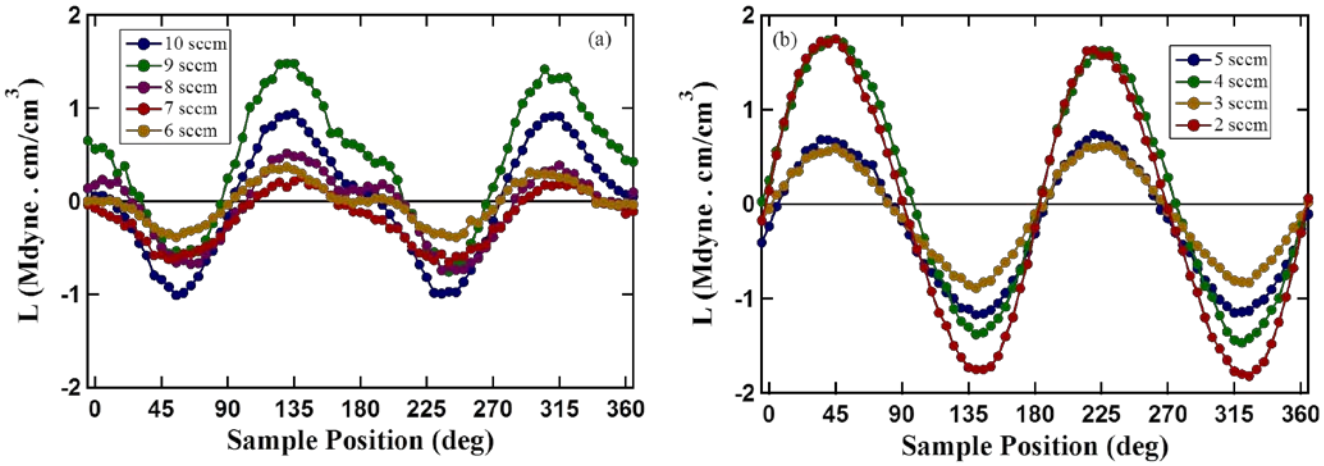

Fig. 3.8 Torque measurement for CFO(111) thin films at a field of 90 kOe with different oxygen flow rate of (a) 10-6 and (b) 5-2 sccm

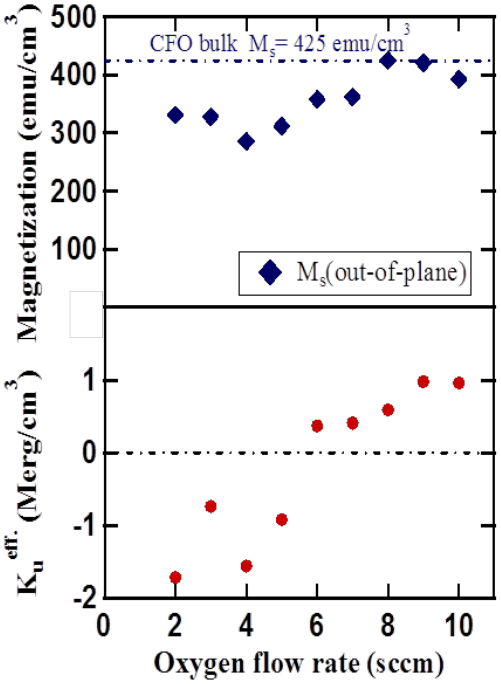

Fig. 3.9 Plot of saturation magnetization (out-of-plane) and effective uniaxial magnetic anisotropy (K_u^{eff}) of CFO(111) thin films vs. oxygen flow rate.

3.5.3 Thickness

Figure 3.10 shows a cross-sectional HRTEM(High-resolution transmission electron microscopy) image of a CFO(111) thin film with a thickness of 9 nm at T_g = 600 ℃ and O_2 = 9 sccm. The CFO(111)$[11\bar{2}]$ zone axis is parallel to the α-Al_2O_3(0001)$[11\bar{2}0]$ substrate. The study of the image was carried out along the $[1\bar{1}0]$ zone axis. Diffraction pattern analysis was based on the fast Fourier transformation (FFT) of both the CFO(111) thin film and the α-Al_2O_3(0001) substrate revealing the single-crystalline pattern of both materials. The high-resolution cross-sectional image suggests the existence of significant roughness at the interface. Any perturbation in a flat interface produces a highly elastic distortion that is not energetically favorable. On the other hand, if the interface morphology is faceted, lower distortion energy is observed [48].

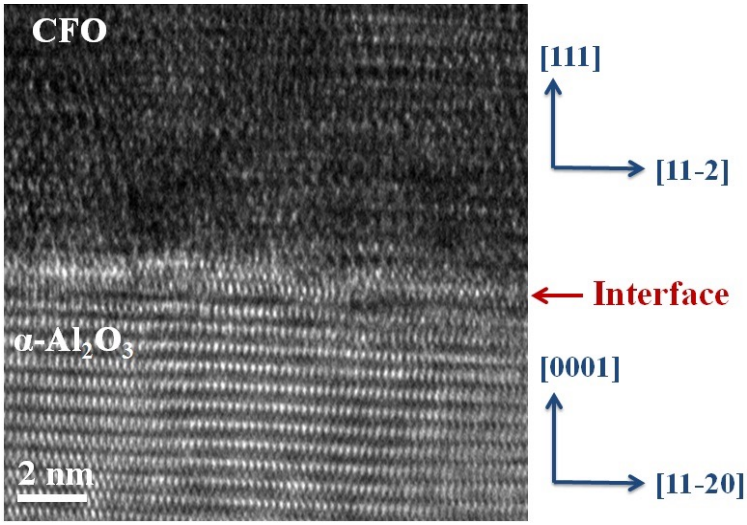

Fig. 3.10 Cross-sectional HRTEM image of CFO(111) thin film with a thickness of 9 nm at 600 ℃ and O_2 = 9 sccm.

The thickness dependence of the CFO(111) thin film was investigated by studying different samples of 9, 18, 26, 32, and 46 nm thicknesses. Figure 3.11 shows the plot of area magnetization measured in the out-of-plane direction versus film thickness. The magnetic squareness ratio increases as the thickness increases. The linear least-square fit of the saturation magnetization normalized by the area for different thicknesses indicates a positive intercept on the horizontal axis, suggesting that a magnetic dead layer (MDL) exists in the CFO(111) thin film. The slope of the plot gives an intrinsic magnetization for the CFO(111) thin film of 387 ± 20 emu/cm^3. The thickness of the magnetic dead layer estimated from the intercept is 1.8 ± 1.4 nm. The estimated thickness of the MDL is comparable to or slightly less than that observed in CFO//MgO (001) [10, 30].

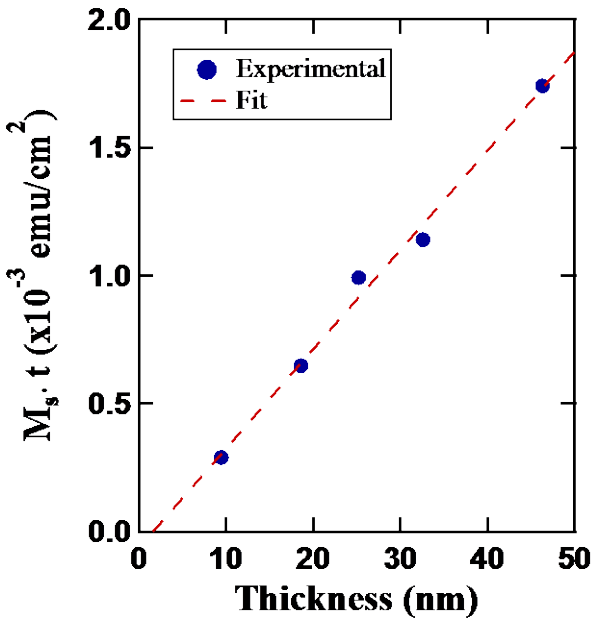

Fig. 3.11 Thickness dependence of the saturation magnetization normalized by area

3.6 Summary of CFO(111) thin films

- $Co_{0.75}Fe_{2.25}O_4$(111) thin films exhibit single-crystalline, epitaxial growth, higher magnetization, and uniaxial magnetic anisotropy.
- A saturation magnetization value M_s = 425 emu/cm^3 (8sccm) was obtained which is the same as the bulk value of CFO, 425 emu/cm^3 [4].
- The perpendicular magnetic anisotropy of CFO(111) thin film at O_2 = 9 sccm is which is slightly lower as compared to CFO(111)//α-Al_2O_3(0001) [23].
- Magnetic squareness ratio increases as the thickness increases. The thickness of the magnetic dead layer estimated from the intercept is 1.8 ± 1.4 nm.

References

1. G. F. Dionne, Magnetic Oxide, (Springe, 2009), pp.151-197.
2. L. W. Martin, Y.-H. Chu, R. Ramesh, Mater. Sci. Eng**.**, **R 68**, 89 (2010).
3. R. O. Handley, Modern Magnetic Materials, (Wiley, New York, 2000), pp.123-131, 179-212.
4. B. D. Cullity and C. D. Graham, Introduction to Magnetic Materials (Wiley, New York, 2009) 2nd ed., pp.175-193, 197-238.
5. A. V. Ramos, J. -B. Moussy, M. -J. Guittet, M. Gautier-Soyer, C. Gatel, P. Bayle-Guillemaud, B. Warot-Fonrose, and E. Snoeck, Phys. Rev. B, **75**, 224421 (2007).
6. J. Moussy, J. Phys. D, **46**, 143001 (2013).
7. F. Sanchez, R. Bachelet, P. de Coux, B. Warot-Fonrose, V. Skumryev, L. Tarnawska, P. Zaumseil, T. Schroeder, and J. Fontcuberta, Appl. Phys. Lett., **99**, 211910 (2011).
8. S. Matzen, J.-B. Moussy, R. Mattana, K. Bouzehouane, C. Deranlot, and F. Petroff, Appl. Phys. Lett., **101**, 042409 (2012).
9. L. Yan, Z. Wang, Z. Xing, J. Li, and D. Viehland, J. Appl. Phys., **107**, 064106 (2010).
10. T. Niizeki, Y. Utsumi, R. Aoyama, H. Yanagihara, J. Inoue, Y. Yamasaki, H. Nakao, K. Koike, and E. Kita, Appl. Phys. Lett., **103**, 162407 (2013).
11. J. C. Slonczewski, Phys. Rev., **110,** 1341(1958).
12. R. M. Bozorth, E. F. Tilden, and A. J. Williams, Phys. Rev., **99**, 1788 (1955).
13. J. C. Slonczewski, J. Phys. Chem. Solids, **15**, 335 (1960).
14. J. Inoue, H. Itoh , M. A. Tanaka, K. Mibu, T. Niizeki, H. Yanagihara, and E. Kita, IEEE Trans. Mag., **49**, 7, 3269 (2013).
15. J. Inoue, H. Yanagihara, and E. Kita, Mater. Res. Express, **1**, 046106 (2014).
16. J. Inoue, T. Niizeki, H. Yanagihara, H. Itoh and E. Kita, AIP Advance, **4**, 027111 (2014).
17. Y. H. Hou, Y. J. Zhao, Z. W. Liu, H. Y. Yu, X. C. Zhong, W. Q. Qiu D. C. Zeng, and L. S. Wen, J. Phys. D: Appl. Phys., **43,** 445003 (2010).
18. D. Odkhuu, P. Taivansaikhan, W. S. Yun, and S. C. Hong, J. Appl. Phys., **115**, 17A916 (2014).
19. J. A. Moyer, C. A. F. Vaz, D. A. Arena, D. Kumah, E. Negusse, and V. E. Henrich, Phys. Rev. B, **84**, 054447 (2011).
20. A. Lisfi, C. M. Williams, L. T. Nguyen, J. C. Lodder, A. Coleman, H. Corcoran, A. Johnson, P. Chang, A. Kumar, and W. Morgan, Phys. Rev. B, **76**, 054405 (2007).
21. Y. Suzuki, G. Hu, R. B. van Dover and R. J. Cava, J. Magn. Magn. Mater., **191**, 1 (1999).

22. W. Huang, J. Zhu, H. Z. Zeng, X. H. Wei, Y. Zhang, and Y. R. Li, Appl. Phys. Lett., **89**, 262506 (2006).
23. J. H. Yin, J. Ding, B. H. Liu, J. B. Yi, X. S. Miao, and J. S. Chen, J. Appl. Phys., **101**, 09K509 (2007).
24. D. Mukherjee, T. Dhakal, M. H. Phan, H. Srikanth, P. Mukherjee, and S. Witanachchi, Physica B, **406**, 2663 (2011).
25. M. Khodaei, S. A. S. Ebrahimi, Y. J. Park, J. M. Ok, J. S. Kim, J. Son, and S. Baik, J. Magn. Magn. Mater., **340**, 16 (2013).
26. M. Khodaei , S. A. S. Ebrahimi, Y. J. Park, S. H. Choi, C. G. Kim, J. Son, and S. Baik, Thin Solid Films, **571**, 62 (2014).
27. M. Khodaei, S. A. S. Ebrahimi, Y. J. Park, S. H. Choi, C. G. Kim, J. Son, and S. Baik, J. Mat. Sci., **48**, 6960 (2013).
28. C.-W. Cho, D. Y. Lee, J. S. Bae, and S. Park, J. Magn. Magn. Mater., **368**, 149 (2014).
29. H. Yanagihara, K. Uwabo, M. Minagawa, E. Kita and N. Hirota, J. Appl. Phys., **109**, 07C122 (2011).
30. H. Yanagihara, Y. Utsumi, T. Niizeki, J. Inoue, and E. Kita, J. Appl. Phys., **115**, 17A719, (2014).
31. L. Yan , Y. Wang, J. Li, A. Pyatakov, and D. Viehland, J. Appl. Phys., **104**, 123910 (2008).
32. C. Gatel, B. Warot-Fonrose, S. Matzen, and J. -B. Moussy, Appl. Phys. Lett., **103**, 092405 (2013).
33. M. A. Tanaka, K. Harada, M. Takemura, K. Mibu, and J. Inoue, J. Appl. Phys., **115**, 17C101 (2014).
34. C. Himcinschi, L. Vrejoiu, G. Salvan, M. Fronk, A. Talkenberger, D. R. T. Zahn, D. Rafaja, and J. Kortus, J. Appl. Phys., **113**, 084101 (2013).
35. X. S. Gao, D. H. Bao, B. Birajdar, T. Habisreuther, R. Mattheis, M. A. Schubert, M. Alexe and D. Hesse, J. Phys. D: Appl. Phys., **42**, 175006 (2009).
36. H. Zheng, J. Wang, S. E. Lofland, Z. Ma, L. Mohaddes-Ardabili, T. Zhao, L. Salamanca-Riba, S. R. Shinde, S. B. Ogale, F. Bai, D. Viehland, Y. Jia, D. G. Schlom, M. Wutting, A. Roytburd, R. Ramesh, Science, **303**, 661(2004).
37. R. V. Chopdekar and Y. Suzuki, Appl. Phys. Lett., **89**, 182506 (2006).
38. L. Fina, N. Dix, J. M. Rebled, P. Gemeiner, X. Marti, F. Perio, B. Dkhil, F. Sanchez, L. Fàbrega and J. Fontcuberta, Nanoscale, **5**, 8037 (2013).
39. D. T. Margulies, F. T. Parker, M. L. Rudee, F. E. Spada, J. N. Chapman, P. R. Aitchison, and A. E. Berkowitz, Phys. Rev. Lett., **79**, 5162 (1997).

40. C. -H. Ma, J. -H. Huang, and H. Chen, Thin Solid Films, **418**, 73 (2002).
41. X. Zheng, J. Li, and Y. Zhou, Acta Mater., **52**, 3313 (2004).
42. S. Kobayashi, The Rigaku Journal, **26**, 1 (2010).
43. K. Inaba, S. Kobayashi, K. Uehara, A. Okada, S. L. Reddy, and T. Endo, Adv. Mater. Phys. Chem., **3**, 72 (2013).
44. C. Gatel, E. Snoeck, V. Serin, and A. R. Fert, Eur. Phys. J. B, **45**, 157 (2005).
45. L. Dong, J. Schnitker, R. W. Smith, and D. J. Srolovitz, J. Appl. Phys., **83**, 1 (1998).
46. M. T. Johnson, P. J. H. Bloemen, F. J. A. den Broeder, and J. J. de Vries, Rep. Prog. Phys., **59**, 1409 (1996).
47. D. C. Jiles and C. C. H. Lo, Sens. Actuators A, **106**, 3 (2003).
48. J. X. Ma, D. Mazumdar, G. Kim, H. Sato, N. Z. Bao and A. Gupta, J. Appl. Phys., **108**, 063917 (2010).
49. E. Kita, T. Niizeki, and H. Yanagihara, The 24th TMRC, **P-18** (2013).

Chapter 4
Barium hexaferrite (0001) thin films

4.1 Introduction

Barium hexaferrite ($BaFe_{12}O_{19}$; BaM) is a magnetic oxide with the magnetoplumbite structure [1]. The crystal structure of barium hexaferrite is hexagonal close-packed (HCP) with oxygen frame work [2]. The chemical formula of hexagonal ferrite is: $M\ Fe^{3+}{}_{12}\ O_{19}$, where M = Sr^{2+}, Ba^{2+}, and Pb^{2+}. The Ba^{2+} and O^{2-} ions are both large, about the same size, and nonmagnetic: they are arranged in a close-packed fashion [3]. The smaller Fe^{3+} ions are located in the interstices. The crystal structure of barium hexaferrite is constituted of close-packed layers formed with four fundamental blocks, S, $S^*(2Fe_3O_4)$, R and $R^*(BaFe_6O_{11})$ among which the S^* and R^* blocks can be obtained simply through the rotation of the S, and R blocks respectively, by 180° with respect to the *c*-axis[1-4] as shown in Fig. 4.1[5]. Thus the structure of the M-type material may be written as S R S* R* or chemically $2(BaFe_{12}O_{19})$, i.e., two formula units per unit cell [2-3].

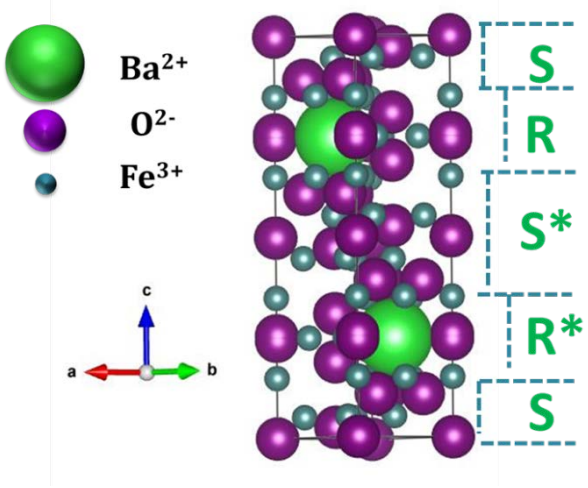

Fig. 4.1 The crystal structure of Barium hexaferrite [5]

Barium hexaferrite ($BaFe_{12}O_{19}$) is widely used as a permanent magnet [1]. Recently, there has been renewed interest in barium hexaferrite thin films for microwave devices and data storage applications, because of its properties such as uniaxial magnetic anisotropy (K_u), moderate saturation magnetization(M_s), high Curie temperature, and low microwave losses [1-4, 6-11].

4.2 Different Growth Techniques

M-type barium hexaferrite thick films grown on single and double-sided of $Gd_3Ga_5O_{12}(111)$ substrates by liquid phase epitaxy have showed higher magnetization (out-of-plane) values[8]. Kresiel *et al* [9] reported that the BaM thin film deposited on $Al_2O_3(0001)$, $Gd_3Ga_5O_{12}(111)$ and

Si(100) substrate have epitaxial, textured and polycrystalline structure. Similarly, BaM thin film grown by chemical vapour deposition on Al_2O_3 substrate showed epitaxial structure, whereas Si/SiO_2 substrate showed polycrystalline structure [10]. The barium hexaferrite thin films deposited by spray pyrolytic method show an increase in magnetization and coercivity as post-annealing temperature (650-900 ℃) increases [11].

4.3 Laser Deposition

A barium hexaferrite film deposited on Al_2O_3(0001) substrate showed with increasing thickness, increased magnetization and decreasing coercivity [12]. Lisfi *et al* reported that the barium hexaferrite deposited on SiO_2/Si substrate with different thickness shows different torque curves due to the tilt of the c-axis [13]. On the other hand, BaM thick film deposited on single crystal SiC substrate with different oxygen pressure showed low remanence at low pressure and high remanence at high pressure [14]. Similarly, barium hexaferrite thick film deposited on sapphire(0001) substrate with and without oxygen showed perpendicular and random orientation magnetic anisotropy [15]. Barium hexaferrite thick film deposited on sapphire (1102) substrate showed hexaferrite and non-hexaferrite mixed phases, with improved magnetization upon laser annealing [16]. Moreover, the barium hexaferrite thick film deposited on c-axis sapphire substrate showed 10% decrease in magnetization as compared to the bulk BaM (M_s= 380 emu/cm^3) [17]. The a-plane sapphire (110-2) substrate used to grown c-axis oriented barium hexaferrite films have in-plane magnetic anisotropy [18]. Saraf *et al* reported that the BaM thick films deposited on sapphire (0001) have perpendicular magnetic anisotropy and narrow FMR lines [19]. Oliver *et al* studied the BaM thin films deposited on a sapphire (0001) substrate by PLD at different oxygen pressures [20]. The obtained saturation magnetization values were slightly lower than bulk values of M_S = 380 emu/cm^3 [3], while the uniaxial magnetic anisotropy energy was comparable to bulk [20].

4.4 Sputtering

Barium ferrite thin film on Si substrate with stoichiometric target showed barium deficiency due to diffusion and to compensate, a barium-rich target was used to increases the magnetization [21]**.** BaM films deposited on alumina and silicon substrate showed random orientation even after post annealing at 800 ℃ [22]. Multilayer and single layer BaM thick film deposited on Si(111), showed improved c-axis orientation with multilayer [23]. On the other hand, the BaM thick film deposited on sapphire (0001) with multilayer films showed easy magnetization perpendicular to the films [24]. Also, Sun *et al* showed the bilayer BaM film has better c-axis orientation and the easy axis of magnetization is perpendicular to the film [25]. Thickness dependence studies showed that

BaM//sapphire (0001) film could change the magnetization from perpendicular to In-plane with increasing thickness [26]. Moreover, In-plane oriented BaM//sapphire(11-20) film is dependent on oxygen pressure and without oxygen pressure shows random orientation [27]. Also, Xu *et al* reported that the composition ratio of the BaM thin films changes depending on sputtering pressure [28]. Coercivity and the remanent ratio increase with decreasing pressure [28].

4.5 Buffer and Multilayer

The BaM film deposited on Pt buffer underlayer on Si(111) substrate showed buffer layer thickness dependence on c-axis orientation [29]. Zheng *et al* deposited BaM film on Pt//MgO(111) substrate and showed the effect of annealing temperature on phase transformation of hexagonal ferrite to spinel ferrite in the XRD pattern [30]. They did a similar study with and without Pt buffer layer on Al_2O_3(0001) substrate showed that the BaM thin film magnetization increase with the presence of the Pt buffer layer [31]. Wang *et al* suggested that the BaM thick film deposited on MgO(111) substrate by liquid phase epitaxy method has lower magnetization and squareness [32]. Similarly, the BaM thin film on MgO//Si(100) showed that the increase in substrate temperature increases with the magnetization of the thin film but remains very low as compared to bulk value [33]. Epitaxial growth of BaM thin film on MgO(111) buffer layer on SiC(0001) substrate showed M_s = 350 emu/cm^3 and narrow FMR line width of 96 Oe , which might be useful for microwave applications [34]. Shinde *et al* suggested improvement in spin waves resonance in barium hexaferrite thin films by using a buffer under layer of $SrAl_5Fe_7O_{19}$ //Al_2O_3(0001) [35]. Morisako *et al* suggested that the BaM films deposited on a buffer layer of AlN and amorphous-BaM, will show low coercivity (due to small grain size) and higher magnetization in case of amorphous-BaM underlayer [36]. The barium hexaferrite thin films deposited on the buffer layer of $Ba_{0.5}Sr_{0.5}TiO_3$ showed reduction in magnetization as compare to film grown directly on a sapphire substrate [37].

4.6 Doping of BaM film

Scandium doped barium hexaferrite films deposited on a-plane sapphire (11-20) showed in-plane magnetic anisotropy and lower magnetization value as compare to bulk BaM [38]. Chen *et al* reported that aluminum doped barium hexaferrite films deposited on Pt/TiO_2/SiO_2/Si substrate by sol-gel method show an out-of-plane easy axis of magnetization and decrease in magnetization as the content of aluminum increases [39].

The overall findings suggest that the saturation magnetization remains relatively low in the thin film; the reason for such a low value is not well understood. For application purposes, high-quality

thin film growth technique is required to achieve large magnetization comparable to the bulk. Thus, the purpose of my research was to understand the effect of composition on the magnetic behavior of the barium hexaferrite (0001) thin films.

4.7 Experimental procedure

The epitaxial growth of barium hexaferrite (0001) thin films was performed with two different target composition (stoichiometric: $BaFe_{12}O_{19}$, and barium-rich: $BaFe_{10}O_x$) on an α-Al_2O_3 (0001) substrate via radio frequency (RF) magnetron sputtering. Hereafter, we refer to the samples grown with the stoichiometric target as BaM1(0001) and with the Ba-rich target as BaM2(0001). The flow rate of Ar was 10 sccm; total pressure inside the sputtering chamber was maintained at 0.4-0.5 Pa. The RF power of the stoichiometric and barium-rich target was set at 100 W and 50 W. The BaM2(0001) thin films of 23.5, 54.7, 73.6, 104, and 140 nm thicknesses were deposited, films of similar thickness (t) were also deposited with BaM1(0001). Both BaM(0001) thin films were post-annealed in atmosphere at 1000 ℃ for 10 minutes.

4.8 Result and Discussion

4.8.1 Film structure and composition

The typical RHEED patterns of the α-Al_2O_3(0001) substrate and the as-grown and post-annealing BaM thin films are shown in Fig. 4.2(a) and (b-c). The RHEED patterns of the epitaxial BaM thin films as grown and post annealed showed sharp and clear streak patterns implying that the BaM thin film has an atomically smooth surface.

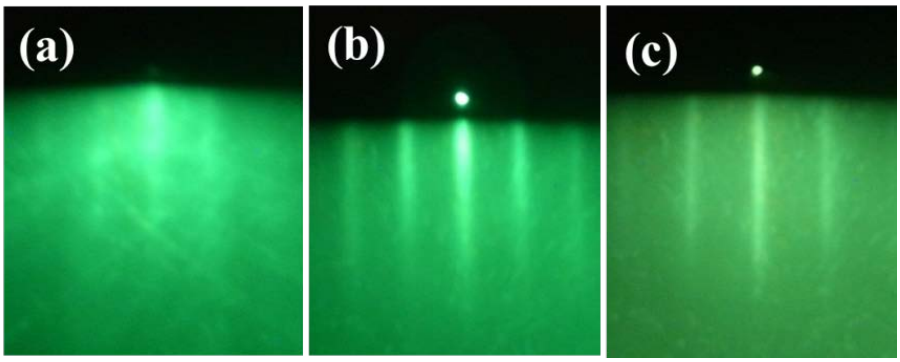

Fig. 4.2 The typical RHEED patterns of the (a) α-Al_2O_3(0001) substrate and (b-c) the as-grown and post-annealing BaM2 thin films.

Figure 4.3 shows typical θ-2θ XRD patterns for BaM2 thin films with thicknesses of 23.5, 54.7, 73.6, 104, and 140 nm. The dominant reflection peaks of BaM are (006), (008) and (0014), indicating excellent c-axis orientation. However, at a larger thickness of 140 nm, the BaM2(0001)

thin film shows additional peaks assigned as (105), (207), and (315) with very low intensity. At the higher thickness of 140 nm, texture or polycrystalline pattern is seen rather than a single crystalline pattern because of the change in growth mode.

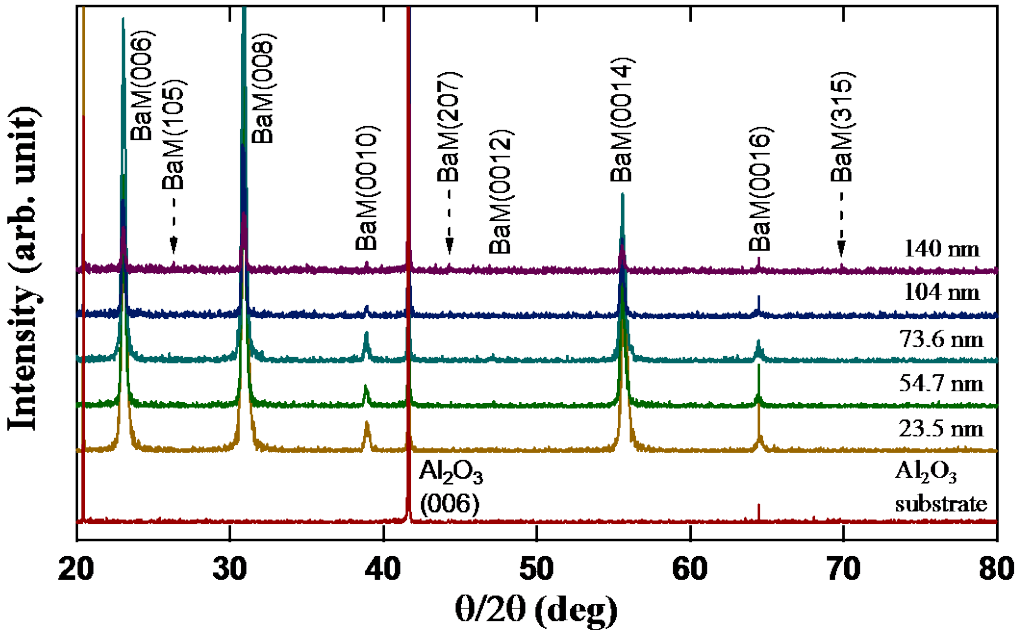

Fig. 4.3 The typical θ/2θ XRD patterns for BaM2(0001) thin films with thicknesses of 23.5, 54.7, 73.6, 104, and 140 nm.

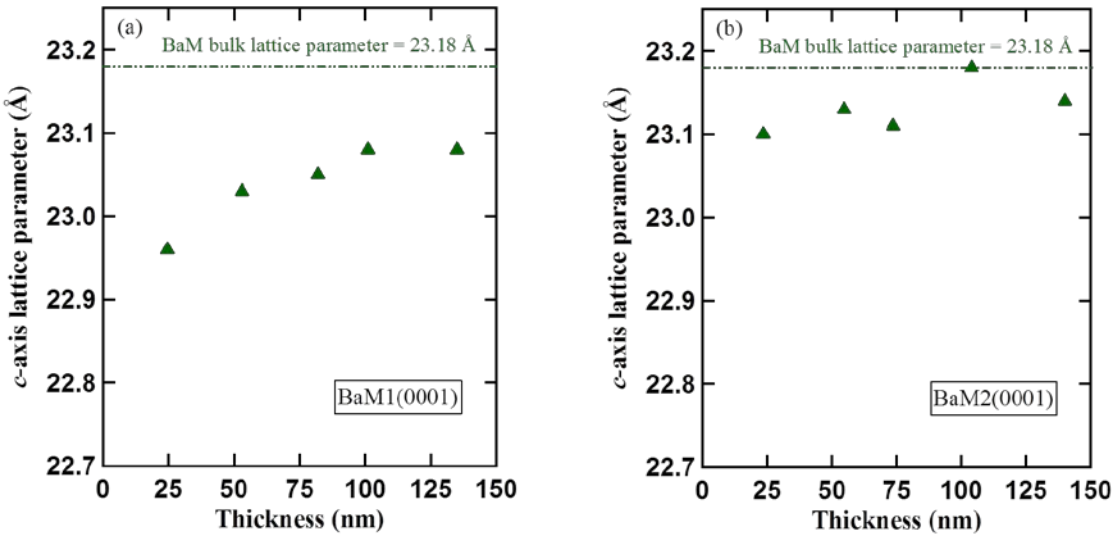

Fig. 4.4 Film thickness dependence of the measured out-of-plane lattice parameters of epitaxial (a) BaM1(0001) and (b) BaM2(0001) thin films grown on α-Al_2O_3(0001) substrates.

It is also found that the value of the lattice parameter c of the BaM thin films deviates from its bulk value of 23.18 Å [ICDD PDF 01-084-0757] as shown in Fig. 4.4(a-b). In all samples of

BaM1(0001) thin films using the position of the (008) Bragg peak, the obtained value was lower in the range of 23.0 to 23.1 Å, but in the case of BaM2(0001) thin films for all samples, the obtained values ranged from 23.1 to 23.2 Å.

Figure 4.5 shows the in-plane $2\theta_\chi$ scans used to determine the in-plane epitaxial relationship. The epitaxial relationship was BaM2[110](001) ‖ α-Al_2O_3[100](001). The lattice mismatch between BaM and α-Al_2O_3 was calculated as 7% from the bulk values of the interplanar spacing of $d_{\mathrm{BaM}\ (22\,0)} = a/4$ Å [a = 5.892 Å (ICDD No. 01-084-0757)] and $d_{\alpha-\mathrm{Al_2O_3}\ (3\,0\,0)} = a/2\sqrt{3}$ Å [a = 4.758 Å (ICDD No. 00-046-1212)]. Since sapphire and BaM have different crystal symmetry, the lattice mismatch could not be ascertained directly. However, by comparing the areas of the sapphire and BaM oxygen planes, one can obtains a 7% lattice mismatch [40].

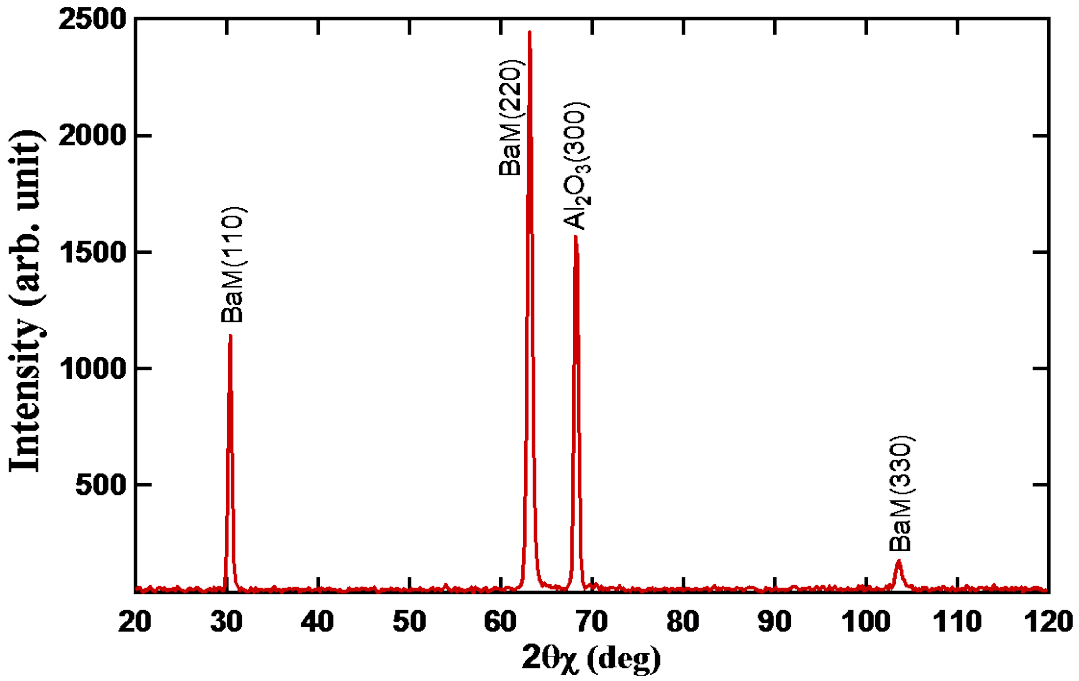

Fig. 4.5 The in-plane 2θχ scans of BaM2 thin films with thickness of 23.5 nm.

RBS was performed to evaluate the composition of the BaM1(0001) and BaM2(0001) thin films as shown in Fig. 4.6 and 4.7. The evaluated off-stoichiometric ratio of Ba:Fe was 1:9 in case of BaM1(0001) thin film, suggesting that some defects exist in the obtained hexaferrite thin films. The RBS result of BaM1(0001) and BaM2(0001) thin films pre and post-annealing as listed in Table 4.1, show that the ratio of Ba:Fe is 1:12. It suggests that the stoichiometric target gives Ba-rich BaM thin films and a Ba-rich target produces stoichiometric BaM thin films.

Table 4.1 The composition ratios of Ba to Fe determined from RBS spectra with two different targets.

Target	Post annealing	RF power (W)	Ba_x	Fe_{13-x}
$BaFe_{12}O_{19}$	Yes	100	1.31	11.69
$BaFe_{10}O_x$	Yes	50	1.07	11.93
$BaFe_{10}O_x$	No	50	1.03	11.97

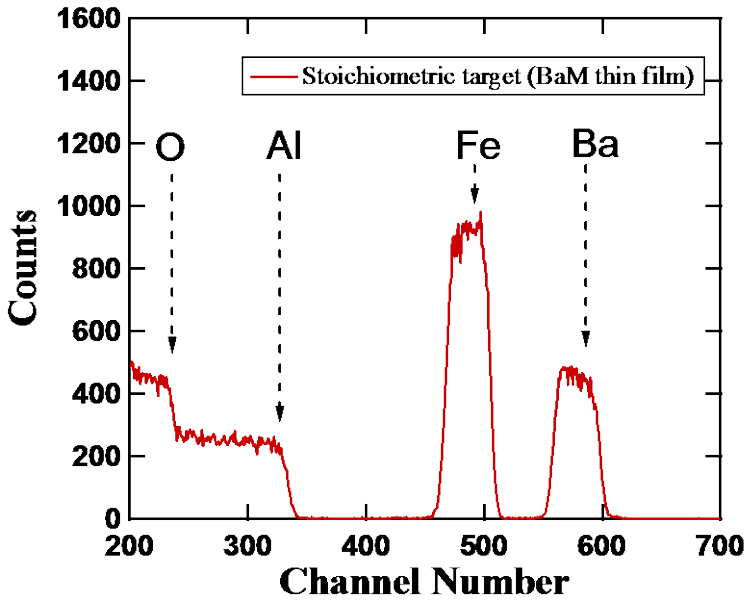

Fig. 4.6 The RBS spectra of BaM1(0001) thin film deposited with stoichiometric target.

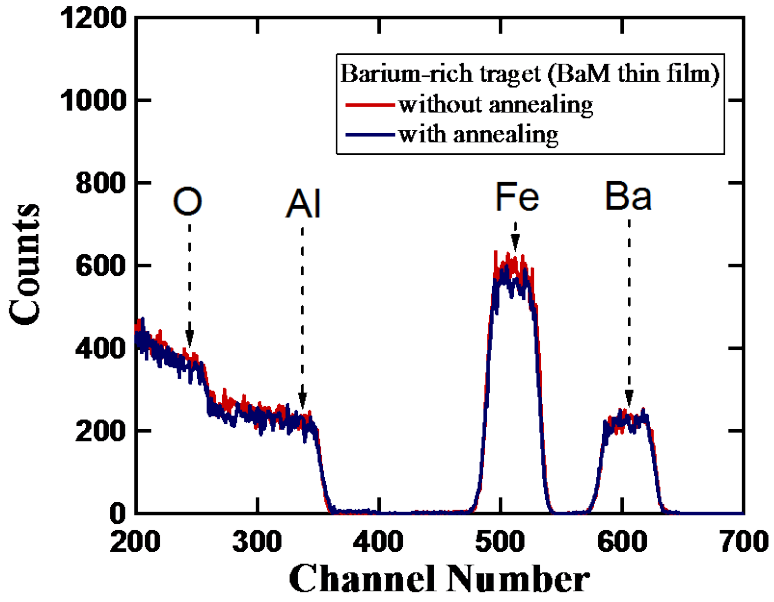

Fig. 4.7 The RBS spectra of BaM(0001) thin film deposited with barium-rich target **(**with and without annealing).

4.8.2 Comparison of magnetic properties of BaM(0001) thin films

4.8.2 (a) Magnetization curve

The magnetization curves of BaM(0001) thin films deposited on α-Al_2O_3(0001) substrate are shown in Fig. 4.8(a-b). The BaM(0001) thin films grown under optimal conditions exhibit magnetic anisotropy with the easy axis of magnetization perpendicular to the films. The BaM1(0001) thin film of thickness 101 nm shows saturation magnetization (out-of-plane) of 304 emu/cm^3, which is less than that of the bulk value of barium hexaferrite (M_s = 380 emu/cm^3) [3]. It is also found that the saturation magnetization of all samples remains at about ~300 emu/cm^3 [BaM1(0001)], and no film thickness dependence is observed. However, the coercive force increases as the film thickness become smaller and the squareness ratio(M_r/M_s) tends to decrease as the film thickness increases in case of BaM1(0001) thin films. But the BaM2(0001) thin films shows increase in magnetization (M_s) increases with increasing thickness and reaches 379 emu/cm^3 (t = 104). The observed M_s is the same as the bulk value of barium hexaferrite (M_s = 380 emu/cm^3) [3].

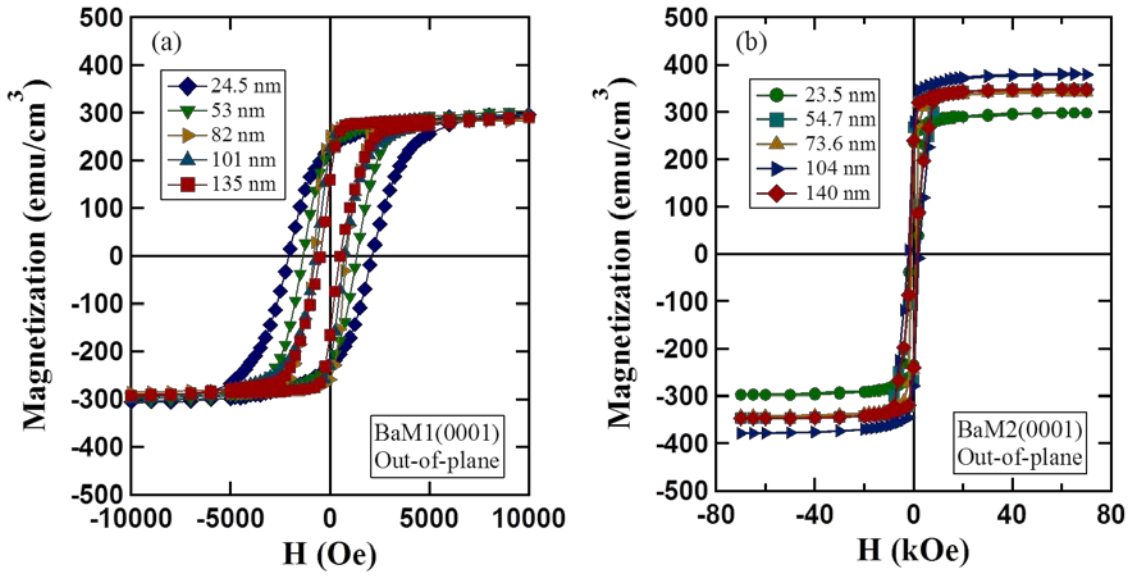

Fig. 4.8 (a-b) The magnetization curves of BaM(0001) thin films deposited on α-Al_2O_3(0001) substrate with various thicknesses

4.8.2 (b) Torque measurement

Figure 4.9 shows the torque measurement of BaM2(0001) thin films at a field of 90 kOe, with different thickness of 23.5, 54.7, 73.6, 104, and 140 nm. The torque curves indicate an easy axis of the uniaxial magnetic anisotropy perpendicular to the film plane, parallel to the *c*-axis. In addition, since all the curves seem to be sinusoidal-like and possess no significant field-dependence, the applied fields are much greater than the anisotropic field of the BaM film.

The uniaxial magnetic anisotropy energy can be written as $E = K_u^{eff} \sin^2\theta$ [2, 3], where K_u^{eff} and θ are effective uniaxial magnetic anisotropy constant and the angle between saturation magnetization M_s and the easy axis, respectively. The observed K_u^{eff} contains magnetic anisotropy contributions from the bulk (K_u) and demagnetization energy ($2\pi M_s^2$), therefore, it is described as $K_u^{eff} = K_u - 2\pi M_s^2$. The intrinsic $K_u = K_u^{eff} + 2\pi M_s^2$ of the BaM2(0001) thin film of 23.5 nm is 3×10^6 erg/cm^3 , which is slightly lower than that of the bulk $K_{u1} = 3.25 \times 10^6$ erg/cm^3 [2, 6].

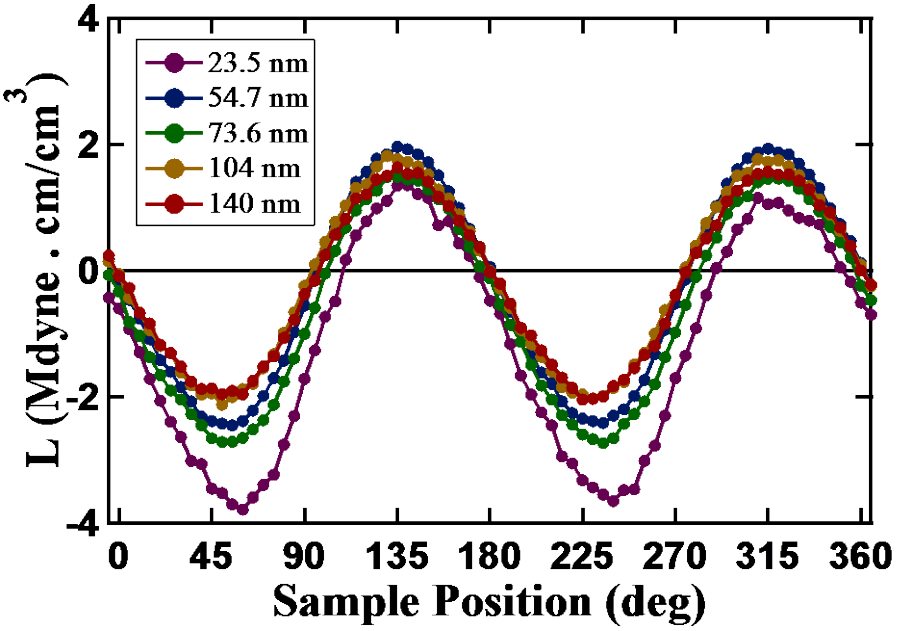

Fig. 4.9 The torque measurement of BaM2(0001) thin films at a field of 90 kOe, with different thickness of 23.5, 54.7, 73.6, 104, and 140 nm.

Fig. 4.10(a-b) shows the saturation magnetization measured along the out-of-plane and K_u of BaM(0001) thin films vs. different thicknesses. The saturation magnetization in the case of BaM1(0001) thin films is almost constant for all film thickness. On the other hand, the K_u decrease with increasing film thickness and becomes almost constant when the film thickness is above 100 nm. The BaM2(0001) thin films K_u also shows similar behavior. But the saturation magnetization in the case of BaM2(0001) thin films increases with film thickness. In both cases the K_u value is large at lower thickness (23 nm), owing to the existence of lattice strain.

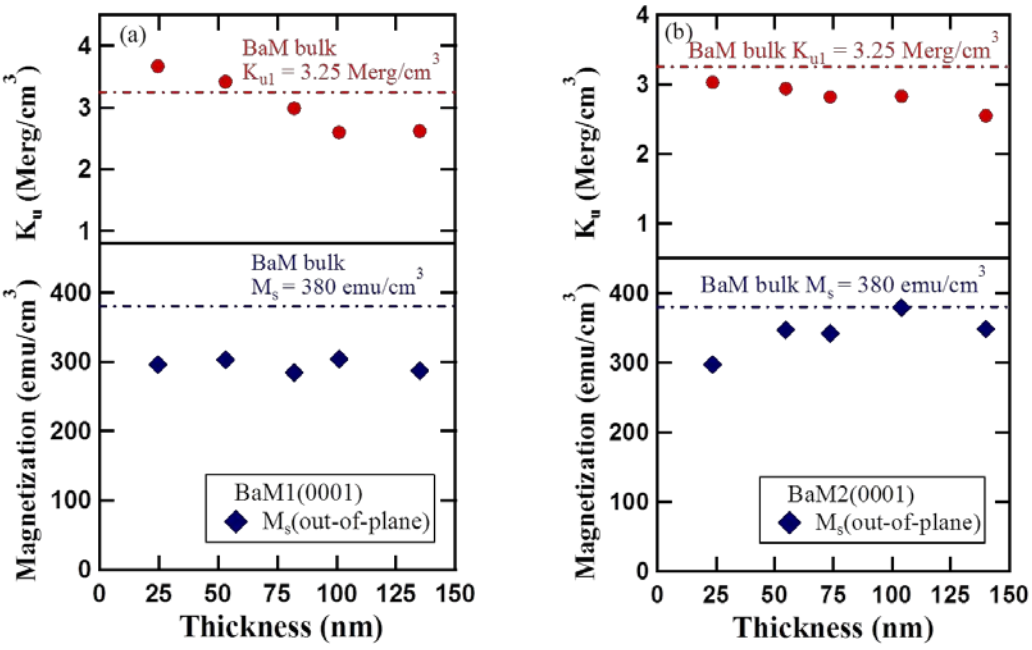

Fig. 4.10 (a-b) The saturation magnetization measured along the out-of-plane and K_u of BaM(0001) thin films vs. different thicknesses

4.8.2 (c) Surface anisotropy

Figure 4.11(a-b) shows the plot between $K_u^{eff} \cdot t$ vs. t. The slope of the plot gives a volumetric component of $K_v - 2\pi M_s^2$ for the BaM(0001) thin film, which is 1.76 ± 0.2 Merg/cm^3 (BaM1(0001)) and 1.64 ± 0.07 Merg/cm^3 (BaM2(0001)). The surface/interface anisotropy estimated from the intercept is 4.4 ± 1.7 erg/cm^2 (BaM1(0001)) and 2.6 ± 1.7 erg/cm^2 (BaM2(0001)). The surface/interface anisotropy obtained is higher in case of BaM1(0001). The estimated surface/interface anisotropy probably originates from either local distortions or modification of the electronic states at the interface.

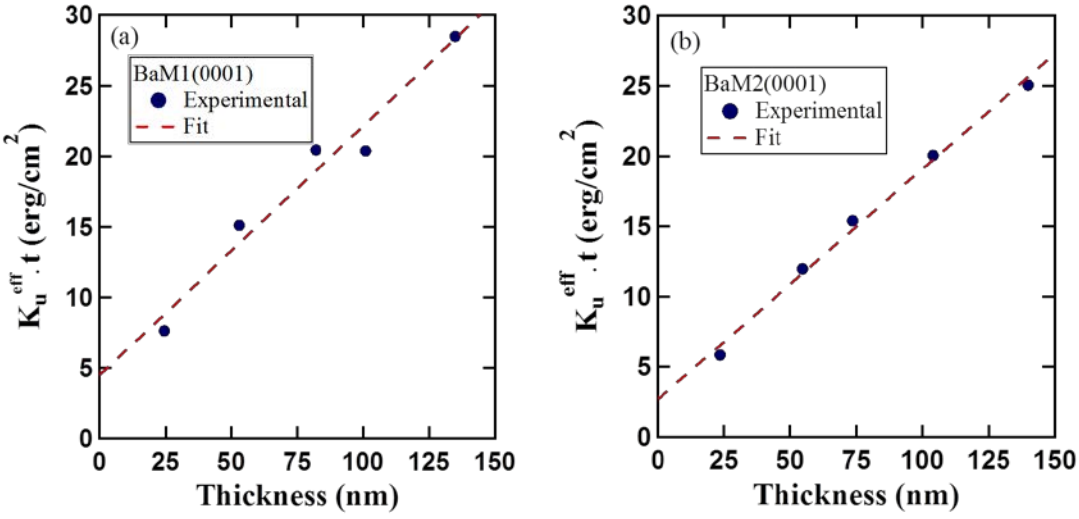

Fig. 4.11 (a-b) The plot between $K_u^{eff} \cdot t$ vs. t.

4.8.2 (d) Magnetic dead layer

Figure 4.12 (a-b) shows the plot of thickness dependence of the saturation magnetization normalized by area. The slope of the plot gives an intrinsic magnetization of 286 ± 11 emu/cm^3 for the BaM1(0001) thin films and 366 ± 19 emu/cm^3. The estimated magnetic dead layer from the intercept is almost zero or negligible in case of BaM1(0001) thin films. But in case of BaM2(0001) thin films the magnetic dead layer estimated from the intercept is 3.8 ± 4.4 nm.

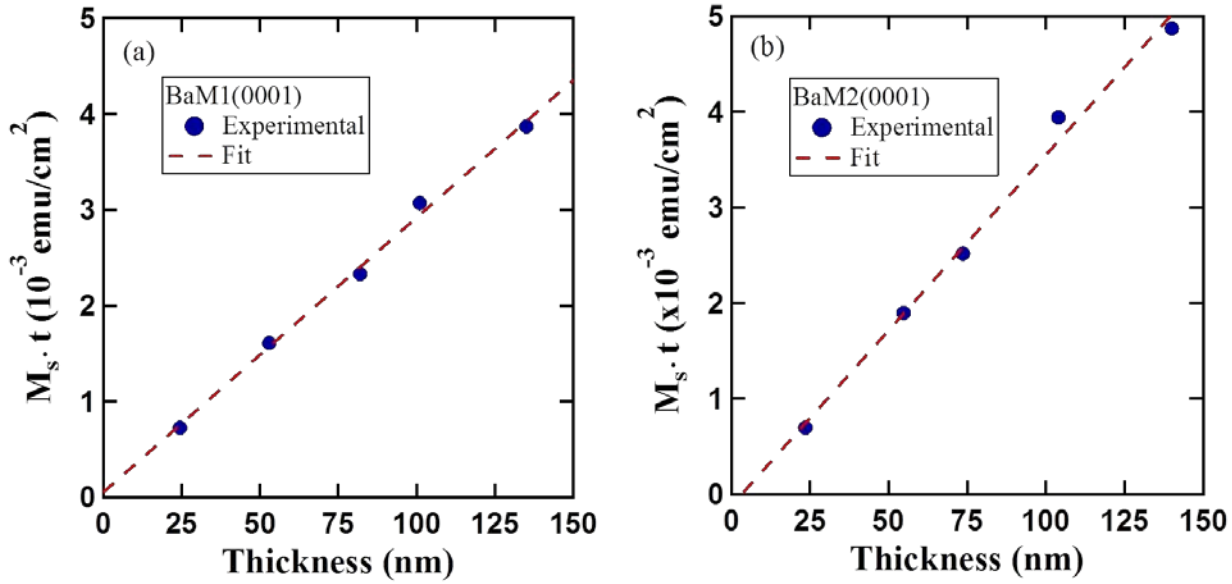

Fig. 4.12 (a-b) The plot of thickness dependence of the saturation magnetization normalized by area.

By using the relation $K_u = K_u^{eff} + 2\pi M_s^2$, the intrinsic magnetic anisotropy is K_u = 2.27 Merg/cm^3 (BaM1(0001)) and 2.48 Merg/cm^3 (BaM2(0001)) (cf. 3.25 Merg/cm^3) .

4.8.3 Reduction of magnetization and magnetic anisotropy in barium-rich thin film

The crystal structure of barium hexaferrite is constituted of close-packed layers formed with four fundamental blocks, S, S*($2Fe_3O_4$), R and R*($BaFe_6O_{11}$) among which the S* and R* blocks can be obtained simply through the rotation of the S, and R blocks respectively, by 180° with respect to the *c*-axis[1-4] Thus the structure of the M-type material may be written as S R S* R* or chemically 2($BaFe_{12}O_{19}$), i.e. two formula units per unit cell [2-3].

Table 4.2 The composition ratios of Ba to Fe determined from RBS spectra with two different targets and saturation magnetizations.

Target	Post annealing	RF power (W)	Ba_x	Fe_{13-x}	M_s (emu/cm^3)
$BaFe_{12}O_{19}$	Yes	100	1.31	11.69	304
$BaFe_{10}O_x$	Yes	50	1.07	11.93	379
$BaFe_{10}O_x$	No	50	1.03	11.97	---

The composition ratios of Ba to Fe determined from RBS spectra by using two different targets, and the corresponding saturation magnetizations are listed in Table 4.2. A pair of S and R or S^* and R^* conserves charge neutrality, and Ba ions occupy the R (or R^*) block. Therefore, an off-stoichiometric M-type hexaferrite may involve another oxide block such as T-block ($Ba_2Fe_8O_{14}$) [1]. If we assume that a pair of S R or S^* R^* blocks are randomly replaced by T-blocks or similar composition ceramics in our films to compensate the Ba-rich composition, there is approximately 20% of T-block in volume. Since T-blocks are composed of Fe^{3+} whose *d*-levels are fully occupied, the contribution to the magnetic anisotropy is supposed to be very weak. Moreover, the magnetic moment of T-block is totally compensated [1]. Therefore, the rest of the $S^{(*)}$ and $R^{(*)}$ blocks only contribute toward the M_s and K_u. Taking account of the existence of the T-block, the expected M_s and K_u are 304 emu/cm^3 and 2.6 Merg/cm^3, respectively, reasonably close to the experimental values of $M_s = 286 \pm 11$ emu/cm^3 and $K_u = 2.27 \pm 0.24$ Merg/cm^3. Therefore, such reduction of M_s and K_u, in off-stoichiometric BaM1(0001) thin films may be explained by randomly existing T-blocks. In order to prove this experimentally we used a barium rich target to grow the barium hexaferrite thin films.

4.9 Summary of BaM(0001) thin films

- The RHEED pattern obtained from the barium ferrite thin film provides evidence of epitaxial growth after deposition and post annealing in case of BaM2(0001) thin films
- The dominant reflection peaks (XRD pattern) of BaM are (006), (008) and (0014), which indicate excellent c-axis orientation.
- The BaM2(0001) thin film (thickness 104 nm) shows M_s (out-of-plane) of 379 emu/cm^3, which is comparably equal to the bulk value of $BaFe_{12}O_{19}$ (380 emu/cm^3).

- The uniaxial magnetic anisotropy of the BaM2(0001) thin film of 23.5 nm is $K_u = 3.03 \times 10^6\ \mathrm{erg/cm^3}$, which is slightly lower than the value of bulk $BaFe_{12}O_{19}$ (3.25 $Merg/cm^3$).
- The composition study revealed that the barium to iron ratio in the deposited thin film is variable.
- RBS study revealed that the stoichiometric barium hexaferrite target produces barium rich BaM thin films, while the barium rich target presents stoichiometric BaM thin films.
- The T-block model successfully explains the existences of extra barium in the BaM1(0001) thin films.
- It also explains the reduction in magnetization and uniaxial magnetic anisotropy in the BaM1(0001) thin films.

References

1. R. C. Pullar, Prog. Mat. Sci**. 57**, 1191(2012).
2. R. O. Handley, Modern Magnetic Materials, (Wiley, New York, 2000), pp.179-212, 485-491.
3. B. D. Cullity and C. D. Graham, Introduction to Magnetic Materials (Wiley, New York, 2009) 2nd ed., pp.175-193, 197-238.
4. M. Wu, M-Type Barium Hexagonal Ferrite Films, Advanced Magnetic Materials, Dr. Leszek Malkinski (Ed.), chapter 2, InTech (2012).
5. http://www.crystallography.net/cod/9008137.htm.
6. B. T. Shirk, and W. R. Buessem, J. Appl. Phys., **40**, 1294 (1969).
7. R. D. Weir, Carl W. Nelson, Vertical-Magnetic-Recording medium with barium ferrite magnetic layer, United States Patent 6110557, 29 (2000).
8. S. D. Yoon and C. Vittoria, J. Appl. Phys., **96**, 4, 2131 (2004).
9. J. Kreisel, S. Pignard, H. Vincent , J. P. Senateur, and G. Lucazeau, Appl. Phys. Lett. **73**, 1194 (1998).
10. S. Pignard, H. Vincent, J. P. Senateur, Thin Solid Films, **350**, 119 (1999).
11. V. K. Sankaranarayanan, R. P. Pant, A. C. Rastogi, J. Magn. Magn. Mater. **220**, 72 (2000).
12. S. R. Shinde, R. Ramesh, S. E. Lofland, S. M. Bhagat, S. B. Ogale, R. P. Sharma, T. Venkatesan, Appl. Phys. Lett., **72**, 3443 (1998).
13. A. Lisfi, J. C. Lodder, C. M. Williams, Appl. Phys. Lett., **83**, 4, 719 (2003).
14. Z. Chen, A. Yang, S. D. Yoon, K. Ziemer, C. Vittoria, V. G. Harris, J. Magn. Magn. Mater. **301**, 166 (2006).
15. A. Lisfi, J. C. Lodder, E. G. Keim and C. M. Williams, Appl. Phys. Lett. **82**, 1, 76 (2003).
16. M. Koleva, P. Atanasov, R. Tomov, O. Vankov, C. Matin, C. Ristoscu, I. Mihailescu, D. Iorgov, S. Angelova, Ch. Ghelev, N. Mihailov, Appl. Surf. Sci., **154-155**, 485 (2000).
17. Y.-Y. Song, S. Kalarickal, and C. E. Patton, J. Appl. Phys., **94**, 8, 5103 (2003).
18. S. D. Yoon C. Vittoria, and S. A. Oliver, J. Appl. Phys., **93**, 4023 (2003).
19. L.V. Saraf, S. E. Lofland, A. V. Cresce, S. M. Bhagat and R. Ramesh, Appl. Phys. Lett., **79**, 3, 385 (2001).
20. S. A. Oliver, M. L. Chen, I. Kozulin, C. Vittoria, J. Magn. Magn. Mater., **213**, 326 (2000).
21. Z. Zhuang, M. H. Kryder, R. M. White, and D. E. Laughlin, Mat. Res. Soc. Symp. Proc., **577**, 605 (1999).
22. S. Capraro, M. L. Berre, J. P. Chatelon, H. Joisten, E. Mery, B. Bayard, J. J. Rousseau, D. Barbier, Sens. Actuators A, **113**, 382 (2004).

23. S. H. Gee, Y. K. Hong, D. W. Erickson, T. Tanaka, And M. H. Park, J. Appl. Phys., **93**, 7507 (2003).
24. Z. Xu, Z. Lan, K. Sun, Z. Yu, X. Jiang, R. Guo, C. Wu, J. Alloys Compd., **575**, 257 (2013).
25. K. Sun, Q. Li, H. Guo, Y. Yang, Z. Yu, Z. Xu, X. Jiang, Z. Lan, L. Li, J. Alloys Compd., **663**, 645 (2016).
26. T. S. Cho, S. J. Doh, J. H. Je and D. Y. Noh, J. Appl. Phys., **86**, 4, 1958 (1999).
27. S. Meng, Z. Yue, L. Li, Mater. Lett., **86**, 92 (2012).
28. H. Xu, W. Zhang, B. Peng, W. Zhang, Appl. Surf. Sci., **257**, 2689 (2011).
29. L. Zhang, X. D. Su, Y. Chen, Q. F. Li, and V. G. Harris, Scripta Mater., **63**, 492 (2010).
30. H. Zheng, M. Han , L. Zheng, J. Deng, P. Zheng, Q. Wu, L. Deng, H. Qin, J. Magn. Magn. Mater., **413**, 25 (2016).
31. H. Zheng, L. Zheng, P. Zheng, J.X. Deng, Z.H. Ying, H.B. Qin, Mater. Lett., **190**, 263 (2017).
32. S. G. Wang, S. D. Yoon and C. Vittoria, J. Appl. Phys., **92**, 6728 (2002).
33. X. H. Liu, M. H. Hong, W. D. Song, G. X. Chen, H. M. J. Lam, J. P. Wang, T. C. Chong, Appl. Phys. A, **80**, 611 (2005).
34. Z. Chen, A. F. Yang, , A. Gieler, V. G. Harris, and C. Vittoria, Appl. Phys. Lett., **91**, 182505 (2007).
35. S. R. Shinde, S. E. Lofland, C. S. Ganpule, S. M. Bhagat, S. B. Ogale, R. Ramesh , T. Venkatesan, Appl. Phys. Lett., **74**, 4, 594 (1999).
36. A. Morisako, T. Naka, K. Ito, A. Takizawa, , M. Matsumoto, Y. K. Hong, J. Magn. Magn. Mater., **242–245**, 304 (2002).
37. S. Srinath, N. A. Frey, R. Heindl, H. Srikanth, K. R. Coffey, and N. J. Dudney, J. Appl. Phys., **97**, 10J115 (2005).
38. S. D. Yoon, C. Vittoria, S. A. Oliver, J. Magn. Magn. Mater. **265**, 130 (2003).
39. D. Chen, Z. Chen, G. Wang, Y. Chen, Y. Li, Y. Liu, J. Magn. Magn. Mater. **444**, 7 (2017).
40. M. S. Yuan, H. L. Glass, and L. R. Adkins, Appl. Phys. Lett., **53**, 340 (1988).

Chapter 5
Conclusions

Reactive RF magnetron sputtering was found to be a useful technique for growing epitaxial thin films of CFO(111) and BaM(0001) on single crystal α-Al_2O_3(0001) substrates. The obtained saturation magnetization and perpendicular magnetic anisotropy in cobalt ferrite and barium hexaferrite thin films were comparable to the bulk. $Co_xFe_{3-x}O_4$ (CFO) (111) epitaxial thin films were grown by optimizing parameters such as growth temperature, oxygen flow rate, and thickness. The optimum growth temperature for CFO(111) thin films was found to be 600 ℃ . The saturation magnetization obtained at growth temperature of 600 ℃ was M_s = 381 emu/cm^3. In the case of oxygen flow rate dependence, the saturation magnetization of the CFO(111) film was 425 emu/cm^3, equal to the bulk value of $CoFe_2O_4$ (425 emu/cm^3) at 8 sccm. Among the films grown at oxygen flow rates of 5 to 2 sccm, we observed a decrease in magnetization, although the XRD and RHEED patterns were similar to those of films grown at higher oxygen flow rates. The uniaxial magnetic anisotropy of the CFO(111) thin film at an O_2 flow rate of 9 sccm was $K_u = 2.09 \times 10^6$ erg/cm^3. The magneto-elastic effect theory is used to compare the experimentally obtained PMA value. Moreover, the thickness dependence studied, showed that the thickness of the magnetic dead layer estimated from the intercept was 1.8 ± 1.4 nm.

In addition to that, a barium hexaferrite (0001) thin film is also deposited on the sapphire substrate by using two different target compositions. It suggests that the stoichiometric target gives Ba-rich BaM thin films and a Ba-rich target produces stoichiometric BaM thin films. The barium hexaferrite (0001) thin films grown under optimal conditions exhibited magnetic anisotropy with easy axis of magnetization perpendicular to the films with a high squareness ratio of 0.7. The BaM1(0001) thin film of thickness 101 nm shows saturation magnetization M_s (out-of-plane) of 304 emu/cm^3, while the BaM2(0001) thin film (thickness 104 nm) showed M_s (out-of-plane) of 379 emu/cm^3, which is comparable to the bulk value of $BaFe_{12}O_{19}$ (380 emu/cm^3). The effective uniaxial magnetic anisotropy K_u^{eff} of the BaM1(0001) thin film of 24.5 nm thickness was $K_u^{eff} = 3.12 \times 10^6$ erg/cm^3. On the other hand, BaM2(0001) thin film of 23.5 nm is $K_u^{eff.} = 2.48 \times 10^6$ erg/cm^3. Although the saturation magnetization in case of BaM1(0001) thin films is almost constant for all film thickness, the magnetic anisotropy constant decreases with increasing film thickness and becomes almost constant over 100 nm. But in case of BaM2(0001) thin films, the saturation magnetization get closer to the bulk value with increasing the film thickness. Taking

account of T-blocks into consideration for Ba-rich composition, we try to explain the reduction of magnetization and magnetic anisotropy in the system.

Despite the large lattice mismatch (about ~7-8%) between the thin films and the sapphire substrate, there was no sufficient lattice distortion in the thin films. To realize a stronger PMA in CFO(111) and BaM(0001) thin films, sufficiently large epitaxial stress and strain must be induced using appropriate buffer layers or substrates.

The following future work is thus proposed:

- Studies of magnetization change induced by an electric field in ME thin film heterostructures are required. In this investigation, the CFO and BaM thin films were grown on sapphire substrates, but the AFM thin film between the ferrimagnet and substrate was not investigated.
- The interfacial coupling mechanism such as the exchange bias phenomenon cannot explain sufficiently the properties observed. Hence other coupling mechanisms need to be taken into account, such as the Mauri model [1] and Malozemo model [2-3].
- Reduction of device size and energy requirement is important due to miniaturization of microelectronic devices. Modern technologies of semiconductor fabrication are at nanometer scale and power consumption is in the nanoampere order. Both are important for the realization of electric field control of magnetism in devices.

References

1. D. Mauri, H. C. Siegmann, P. S. Bagus, and E. Kay, J. Appl. Phys., **62**, 3047 (1987).
2. A. P. Malozemoff, Phys. Rev. B, **35**, 7, 3679 (1987).
3. A. P. Malozemoff, J. Appl. Phys., **63**, 3874 (1988).

Appendix

List of symbols

T_C	Curie temperature
T_N	Neel temperature
T_g	Growth temperature
H_{ex}	Exchange bias
H_d	Demagnetizing field
K_u	Uniaxial magnetic anisotropy energy
K_u^{eff}	Effective Uniaxial magnetic anisotropy energy
H	Magnetic field
M	Magnetization
M_s	Saturation magnetization
M_r	Remanent magnetization
H_c	Coercive field
H_s	Saturation field
H_k	Anisotropy field
E	Electric field
σ	Stress
ε	Lattice Strain
P	Electric polarization
Y	Young's modulus
ϵ	Permittivity of the dielectric
χ	Magnetic susceptibility
α	Magneto-electric tensor

List of figures

List of tables

Acknowledgements

First of all, I would like to sincere thanks to Ministry of Education, Culture, Sports, Science, and Technology (MEXT, Japan) for the research student fellowship toward my Ph.D. program and giving me the opportunity to work in Japan. I would like to thanks to my supervisor Prof. Hideto Yanagihara for his continuous guidance and encouragement during my Ph.D. research work. I would also like to thanks to Asst. Prof. Sonia Sharmin for reading and correcting my thesis several times. I would like to thanks to the members of my dissertation committee: Prof. Eiji Kita, Prof. Kazuhiro Hono, Prof. Takashi Suemasu, Prof. Seiji Mitani and Prof. Hideto Yanagihara for generously offering their time, support, guidance and good will throughout the preparation and review of my Ph.D. thesis document.

I would like to express my gratitude to my colleagues Yuki Hisamatsu, Takeshi Tainosho, and Hiroshige Onoda thank you very much for your great support during my Ph.D. research work. Special thanks to Professor Prof. Kazuhiro Hono at NIMS for his support of the SQUID-VSM measurements.

List of publications

1. Magnetic properties of epitaxial barium hexaferrite (0001) thin films deposited by radio frequency magnetron sputtering, Ritesh Patel, Yuma Ikeda, Hiroshige Onoda, Takeshi Tainosho, Yuki Hisamatsu, Sonia Sharmin, Eiji Kita and Hideto Yanagihara, IEEE Transaction on magnetics, vol. 54, 2 (2018).

2. Effect of lattice strain on cobalt ferrite $Co_{0.75}Fe_{2.25}O_4$ (111) thin films, Ritesh Patel, Takeshi Tainosho, Yuki Hisamatsu, Sonia Sharmin, Eiji Kita and Hideto Yanagihara, Japanese Journal of Applied Physics, 56, 053001 (2017)